Stochastic multiscale modeling of the thermomechanical behavior of polycrystalline shape memory alloys

Xuyang Chang, Karine Lavernhe-Taillard, Olivier Hubert

Stochastic multiscale modeling of the thermomechanical behavior of polycrystalline shape memory alloys

Xuyang Chang, Karine Lavernhe-Taillard, Olivier Hubert*

Université Paris-Saclay, ENS Paris-Saclay, CNRS
LMT - Laboratoire de Mécanique et Technologie
61, Avenue du Président Wilson
F-94235 CACHAN Cedex

February 2020

Abstract

A multi-scale model simulating hysteretic thermomechanical behavior of polycrystalline shape memory alloys (SMA) is presented. Using a kinetic Monte-Carlo approach, the energy-based model estimates the stochastic average in terms of volume fraction for a phase or phase variant deriving from the Gibbs free energy density as a selection inside a given population. Indeed pseudo-elastic behavior for example is well-known to be associated with the nucleation of martensite plates inside the austenite parent phase. Associated variants are similar to sub-domains inside a thermodynamic system following the statistical definition of [37]. The germination process of a variant is on the other hand dictated by a germination potential barrier identified from a differential scanning calorimetry (DSC) measurement. The stochastic average for each type of variants inside a grain leads then to the numerical simulation of hysteresis phenomena at the single crystal scale. Homogenization operations allow finally macroscopic quantities (phases fraction, deformation and temperature) to be calculated at the polycrystalline scale. This procedure is applied to model the whole thermomechanical behavior of an equiatomic Ni-Ti SMA polycrystalline alloy considering the phase transformation between austenite, R-phase and martensite.

Keywords— Multi-scale model, Stochastic approach, Kinetic Monte-Carlo, Shape Memory Alloy

1 Introduction

Since the discovery of shape memory effect (SME) in binary nickel-titanium (Ni-Ti) alloy, a major research effort has been focused on the understanding and simulation of the mechanisms associated with the pseudo-elastic behavior in shape memory alloy (SMA) materials. It is now well understood that SME is a particular manifestation of a displacive (diffusionless) solid-solid crystalline phase transformation of a parent phase (denoted as austenite) into a child phase (denoted as martensite). Such transformation occurs under mechanical loading and during the cooling process if initial temperature is sufficiently high so that the parent phase is stabilized. It is also a first order thermodynamic transformation (seen as a change of state) which is characterized by an emission (or absorption) of heat during the transformation. In view of the unique mechanical properties of SMA, their industrial applications are in progress in domains such as microscopic active or passive devices (e.g., actuators, valves) and biomedical tools (e.g., denting). The field of applications remains limited because of the difficulty in obtaining a reliable modeling of their behavior, in particular in case of a multiaxial mechanical or anisothermal situations. This explains the intensive study of SMA behavior and modeling attempts in the last decades. However, the main features that make the modeling of SMA difficult are:

- phase transformations are out-of equilibrium phenomena, as evidenced by the hysteretic character of the transitions.
- latent heat of the transformation modifies the temperature in the neighborhood, and as a result, prevents the transformation to propagate. This induces a localization instability such that the phase distribution is highly contrasted in slender structures [34][11][16].

*Corresponding author, e-mail: olivier.hubert@ens-paris-saclay.fr

Generally, three approaches are proposed to describe the hysteresis thermomechanical phenomena in SMA. First, macroscopic thermomechanical behavior can be obtained in the frame of Generalized Standard Materials by using an average volume fraction of martensite and the associated mean transformation strain as internal variables [1],[25],[24][19]. This approach addresses exclusively the macroscopic scale but laws obtained are in general consistent with thermodynamics and experimental observations. Due to the ad-hoc and phenomenological nature of this approach, relationships between macroscopic response, fundamental material properties and evolution of microstructure during the thermomechanical loading are not provided. Extension to multiaxial loading requires new parameters and a fastidious identification of the transformation thresholds.
The second approach considers the phase transformation at the single crystal scale via an appropriate modeling and uses a scaling process to derive the macroscopic behavior. The local modeling aims at establishing a direct link between hysteretic response and underlying events at different time scales. This approach supposes a more fundamental understanding of the nature of hysteresis phenomena such as meta-stability, micro-instability (localization), material heterogeneity or grain-size induced hysteresis [30][38][26].
The third approach is a mixture between the aforementioned two approaches, seeking to describe the hysteresis phenomena in SMA by adopting the concept of thermodynamic driving force, acting at the boundary between two phases or on an assembly of variants. The force must overcome the level-set germination barrier to propagate. In this type of description, the width of hysteresis loop is directly related to the magnitude of the germination barrier [35][19][18].
In a previous study, the second approach has been adopted by using a uniform stress hypothesis and a Boltzmann type distribution to estimate the volume fraction of austenite and martensite variants under complex thermomechanical loading configurations. The main drawback of this approach was that Boltzmann distribution applies in a reversible thermodynamic framework: out-of equilibrium phenomena during phase transformation were not taken into consideration. This approach however was able to model multiaxial mechanical modeling in an appropriate way.
In this paper, the stochastic and energy based model is reformulated to explore time evolution of volume fraction, aiming at simulating and reproducing the macroscopic hysteresis response and shape memory effect (SME) at the grain and polycrystalline scales[1].

This paper is organized as follows. In section 2, the Gibbs free energy density construction is first recalled. In order to understand and model the source of macroscopic hysteresis, the concept of master equation for calculating the volume fraction of each variant of any phase at the grain scale is introduced. Concepts of meta-stability and germination barrier are then reviewed. In section 3, the Kinetic Monte-Carlo (KMC) framework is detailed. The identification of the modeling parameters (Gibbs free energy parameters, stiffness, mass density, lattice parameters, orientation data) is explained next in section 4: most of them involves a simple Differential Scanning Calorimetry (DSC) measurement. The procedure has been applied to model several aspects of the thermomechanical behavior of an equiatomic Ni-Ti SMA polycrystalline alloy RVE. Modeling the behavior of this material is made particularly delicate by the occurrence of intermediate rhombohedral (R) phase (four variants) involved in the transition from the austenite phase (B2) to the martensite phase (B19') exhibiting twelve variants. Numerical simulations are presented and discussed in section 5. Summary and conclusions are provided in section 6.

[1]Polycrystal is considered as a Representative Volume Element (RVE)

Nomenclature

$\hat{f}(\xi, t)$	Volume fraction of configuration ξ at time instant t
α_v	Volumetric dilatation coefficient (K^{-1})
$\Delta\epsilon_{tr}$	Transformation strain variation
$\gamma(\mu, t)$	Total amount of variants submitted to a μ type transformation at instant t
κ	Thermal conductivity ($W.m^{-1}.K^{-1}$)
$\mathfrak{f}$	Helmholtz free energy density ($J.m^{-3}$)
$\mathfrak{g}$	Gibbs free energy density ($J.m^{-3}$)
$\mathfrak{u}$	Internal energy density ($J.m^{-3}$)
g	Grain or single crystal
RVE	Representative Volume Element - polycrystal
μ	First transformation type
ϕ	phase
ψ	Volume fraction of a phase
ρ	Mass density ($kg.m^{-3}$)
τ	First transformation time (s)
$\boldsymbol{\epsilon}$	Strain Tensor
$\boldsymbol{\sigma}$	Stress Tensor ($N.m^{-2}$)
$\mathbb{C}$	Stiffness matrix ($N.m^{-2}$)
$\vec{q_s}$	The heat flux vector
ξ	Configuration describing the state of grain
$\zeta(t)$	Total amount of variants transformed at instant t
c	Transformation Rate
c_p	Specific heat capacity($J.kg^{-1}.K^{-1}$)
$d\mathfrak{g}^a(i, j)$	Mechanical incompatibility related germination energy barrier between variant i and j ($J.m^{-3}$)
$d\mathfrak{g}^c(dt)$	Metastable germination energy barrier ($J.m^{-3}$)
f	Volume fraction
h	Enthalpy density ($J.m^{-3}$)
i	Digit indicating a variant of type i
k	Equivalent convection factor ($W.m^{-3}.K^{-1}$)
k_b	Boltzmann constant ($J.K^{-1}$)
L_{ij}	Latent heat density associated with a μ type transformation from variant j to variant i ($J.m^{-3}$)
$M(i, j)$	Markov transition matrix from variant j to variant i
N	Number of standard unit inside a grain
n	Number of variant types inside a grain
N_i	Number of standard unit corresponding to a variant i
$p(\tau, \mu)$	Transition probability that a μ type transformation occurs at instant $t + \tau$
$p_1(\tau)$	Transition probability that at least one variant transforms into another in time interval $[t, t + \tau]$
$p_2(\mu\|\tau)$	Transition probability that a μ type transformation occurs for a variant in time interval $[t, t + \tau]$
s	Entropy density ($J.K^{-1}.m^{-3}$)
t	Time (s)
T	Temperature (K)
V_u	Volume of standard unit (m^3)
X	Thermodynamic force associated to ϕ (J/m^3)

2 Multiscale stochastic formulation

In this section, the Gibbs free energy density $\mathfrak{g}$ at the variant scale in SMA is fist defined. Boltzmann system and associated master equation defining the evolution of variant's volume fraction at the grain scale are then introduced.

2.1 Multiscale approach

The scale organization is illustrated in Figure 1, from the variant scale to the RVE scale. The idea of multiscale approach is to use the volume fraction of variant i at time t in a phase ϕ ($f_\phi(i,t)$) or a grain g ($f_g(i,t)$) to describe the physical quantities at different scales and times by appropriate averaging operations. A multiscale approach supposes on the other hand an appropriate *localization* of loading. This step is strongly simplified in the present paper by using an hypothesis of homogeneous loading. In the following, a single crystal or grain g is supposed to be composed of several phases ϕ (austenite, martensite, etc). Hereafter, i denotes a variant meaning that a phase ϕ may be composed of different variants i depending on the crystal symmetry. i is the lowest scale. A single crystal may contain n different variants i in total (sum of all variants in all phases): $i = 1, 2, \cdots n$.

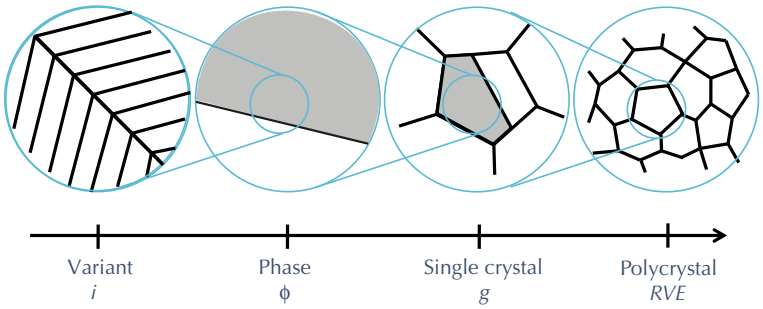

Figure 1: Scales involved in the multiscale modeling of SMA from variant to polycrystal scales.

The statistic description needs to define a Standard Unit (SU) defining the statistic volume (V_u). As for the phase or grain, this volume may be occupied by a fraction of each variant i at time instant t, written simply as $f(i,t)$. The total volume occupied by variant i can be described by a number $N_i(t)$ of unit volume V_u too. Indeed $N_i(t)$ is time dependent, due to variant to variant or phase to phase transition. At time instant t, the total population of SU inside the grain is considered as fixed and noted as N, verifying:

$$N = \sum_{i=1}^{n} N_i(t) \tag{1}$$

leading to a discrete definition of volume fraction of variant i at the grain scale:

$$f_g(i,t) = \frac{N_i(t)}{N}, \ i = 1, 2, \cdots n \tag{2}$$

with

$$\sum_{i=1}^{n} f_g(i,t) = 1 \tag{3}$$

An energy-based stochastic approach is next proposed to define the time evolution of the variants' volume fraction as function of thermal and mechanical loading.

2.2 Definition of the Gibbs free energy density at the variant scale

The first principle given at the local scale states that the total energy density composed of kinetic energy density and internal energy [J m^{-3}] can only be modified by the action of external work and heat flux. The internal energy density at the variant scale is written as $\mathfrak{u}$. At constant velocity, kinetic energy remains as a constant. There is a direct relationship between the variation of internal energy density and heat sources:

$$d\mathfrak{u}(i, s, \boldsymbol{\epsilon}) = dh(i) + T(i)ds(i) + \boldsymbol{\sigma}(i) : d\boldsymbol{\epsilon}(i) \tag{4}$$

This expression is composed of:

- $dh(i)$: chemical energy variation= bound energy variation inside a variant;
- $T(i)ds(i)$: heat quantity variation (thermal power), function of entropy variation ds (second law of thermodynamics) and local temperature T;
- $\boldsymbol{\sigma}(i) : d\boldsymbol{\epsilon}(i)$: mechanical energy variation (mechanical power), function of deformation variation $d\boldsymbol{\epsilon}$ and local stress $\boldsymbol{\sigma}$.

The free (Helmholtz) energy density $\mathfrak{f}(i)$ is a result of the Legendre transformation of internal energy density by heat quantity. It allows energy variation to be defined as function of temperature variation instead of entropy variation:

$$\mathfrak{f}(i,T) = \mathfrak{u}(i,s) - T(i)s(i) \tag{5}$$

The Gibbs free energy (or free enthalpy) is the result of a Legendre transformation of the Helmholtz free energy density by a mechanical quantity. It allows finally the energy variation to be defined as function of stress variation instead of deformation variation.

$$\mathfrak{g}(i,T,\boldsymbol{\sigma}) = \mathfrak{f}(i,T) - \boldsymbol{\sigma}(i) : \boldsymbol{\epsilon}(i) \tag{6}$$

The variation of Gibbs free energy density is given by:

$$d\mathfrak{g}(i,T,\boldsymbol{\sigma}) = dh(i) - s(i)dT(i) - \boldsymbol{\epsilon}(i) : d\boldsymbol{\sigma}(i) \tag{7}$$

A second order Taylor expansion of entropy leads to derive $s(i)$ as function of temperature T, reference entropy s_0 at the reference temperature T_0, mass density ρ and specific heat capacity c_p (considered as temperature independent):

$$s(i,T) = s_0(i,T_0) + \rho(i)c_p(i)ln\left(\frac{T_0(i)}{T(i)}\right) \tag{8}$$

On the other hand, in the framework of small perturbation hypothesis, we wish to consider total deformation $\boldsymbol{\epsilon}(i)$ as a sum of elastic $\boldsymbol{\epsilon}_e(i)$, thermal $\boldsymbol{\epsilon}_{th}(i)$ and transformation $\boldsymbol{\epsilon}_{tr}(i)$ deformations associated with phase transition. The total deformation at the variant scale i can be expressed as function of stress, temperature and $\boldsymbol{\epsilon}_{tr}(i)$ (considered as a *free* deformation) following:

$$\boldsymbol{\epsilon}(i,T,\boldsymbol{\sigma}) = \mathbb{C}^{-1}(i) : \boldsymbol{\sigma}(i) + \frac{\alpha_v(i)}{3}(T(i) - T_0(i))\boldsymbol{I} + \boldsymbol{\epsilon}_{tr}(i) \tag{9}$$

$\mathbb{C}$ is the local stiffness tensor, α_v is the volumetric dilatation coefficient and $\boldsymbol{I}$ the second order identity tensor. The transformation strain $\boldsymbol{\epsilon}_{tr}$ is usually considered as stress independent (and is assumed to be so).
Gibbs free energy density is finally expressed (for a constant) after integration as a formal sum of thermal part $\mathfrak{g}_t(i,T)$, mechanical part $\mathfrak{g}_m(i,\boldsymbol{\sigma})$ and coupled thermomechanical part $\mathfrak{g}_{tm}(i,T,\boldsymbol{\sigma})$.

$$\mathfrak{g}(i,T,\boldsymbol{\sigma}) = \mathfrak{g}_t(i,T) + \mathfrak{g}_m(i,\boldsymbol{\sigma}) + \mathfrak{g}_{tm}(i,T,\boldsymbol{\sigma}) \tag{10}$$

with

$$\begin{aligned}
\mathfrak{g}_t(i,T) &= h(i) - s_0(i)T(i) + \rho(i)c_p(i)\left[T(i) - T_0(i) - T(i)ln\left(\frac{T(i)}{T_0(i)}\right)\right] \\
\mathfrak{g}_m(i,\boldsymbol{\sigma}) &= -\frac{1}{2}\boldsymbol{\sigma}(i) : \mathbb{C}^{-1}(i) : \boldsymbol{\sigma}(i) - \boldsymbol{\sigma}(i) : \boldsymbol{\epsilon}_{tr}(i) \\
\mathfrak{g}_{tm}(i,T,\boldsymbol{\sigma}) &= -\frac{\alpha_v(i)}{3}(T(i) - T_0(i))tr(\boldsymbol{\sigma}(i))
\end{aligned} \tag{11}$$

where $tr(\boldsymbol{\sigma})$ denotes the trace of the stress tensor.

The main simplifications that can be made at this step concern the ad-hoc loading. We will consider in the following that:

- by adopting the Reuss approach for the homogenized medium, stress is supposed as homogeneous over the RVE, leading to: $\boldsymbol{\sigma}(i) = \boldsymbol{\sigma}$;
- temperature is considered homogeneous over the RVE, leading to: $T(i) = T$;
- stiffness, mass density, specific heat capacity and dilatation coefficient are considered as the same for all phases and variants: $\mathbb{C}(i) = \mathbb{C}$, $\rho(i) = \rho$, $c_p(i) = c_p$ and $\alpha_v(i) = \alpha_v$.

The Gibbs free energy density simplifies into:

$$\begin{aligned}\mathfrak{g}(i, T, \boldsymbol{\sigma}) = \quad & h(i) - s_0(i)T + \rho c_p \left[T - T_0 - Tln\left(\frac{T}{T_0}\right)\right] - \frac{1}{2}\boldsymbol{\sigma} : \mathbb{C}^{-1} : \boldsymbol{\sigma} \\ & -\boldsymbol{\sigma} : \boldsymbol{\epsilon}_{tr}(i) - \frac{\alpha_v}{3}(T - T_0)tr(\boldsymbol{\sigma})\end{aligned} \tag{12}$$

2.3 Boltzmann system and master equation

In the Boltzmann stochastic theory, a Boltzmann system is referred as a specific system consisting of N different independent units (N Standard units), where each unit has no interaction with others and total population of units remains unchanged. For simplicity reasons, we firstly consider a system containing one standard unit $N = 1$. This simple system may contain n discrete Gibbs free energy level at time instant t ($\mathfrak{g}(i, t), i = 1, 2 \cdots n$). Consequently the conservation of population in the standard unit can be expressed as:

$$\sum_{i=1}^{n} \frac{df(i,t)}{dt} = 0 \tag{13}$$

As a result, the temporal variation of volume fraction for variant i at time t, $\frac{df(i,t)}{dt}$ can be calculated via a Master equation, which is defined by the following system of equations:

$$\frac{df(i,t)}{dt} = -f_{\mathrm{d}}(i,t) + f_{\mathrm{b}}(i,t) \tag{14}$$

$$\frac{df(i,t)}{dt} = -\sum_{j=1, j\neq i}^{n} \mathrm{Tr}(i,j) f(i,t) + \sum_{j=1, j\neq i}^{n} \mathrm{Tr}(j,i) f(j,t) \tag{15}$$

$$f_{\mathrm{b}}(i,t) = \sum_{j=1, j\neq i}^{n} \mathrm{Tr}(j,i) f(j,t) \tag{16}$$

$$f_{\mathrm{d}}(i,t) = \sum_{j=1, j\neq i}^{n} \mathrm{Tr}(i,j) f(i,t) \tag{17}$$

$$\mathrm{Tr}(i,j) = \min(1, c_{ij} \exp(-\beta_s(\mathfrak{g}(j,t) - \mathfrak{g}(i,t)))) \tag{18}$$

$$\beta_s = \frac{V_u}{k_b T} \tag{19}$$

$\frac{df(i,t)}{dt}$ indicates the temporal increment of volume fraction for variant i, which is determined by the difference between birth amount $f_{\mathrm{b}}(i,t)$ and death amount $f_{\mathrm{d}}(i,t)$;

$f_{\mathrm{b}}(i,t)$ and $f_{\mathrm{d}}(i,t)$ are the birth and death amount for the volume fraction of variant i. These two amounts are both determined by the transition probability function $\mathrm{Tr}(i,j)$ and the current volume fraction of the system $f(i,t)$ (Equation 16 and Equation 17);

$\mathrm{Tr}(i,j)$ is the transition probability, defining the probability for variant i to transform towards variant j;

β_s is a parameter that defines the severity of transformation (Equation 17). It is calculated from the unit volume V_u, current temperature T and Boltzmann constant k_b;

c_{ij} is the transformation rate of variant i towards variant j.

In order to simplify the Master equation, we decide to adopt the Markov convention. The Markov transition matrix $M(i,j)$ verifies:

$$M(i,j) = \mathrm{Tr}(i,j), \forall (i,j), i \neq j$$
$$M(i,i) = -\sum_{j=1}^{n} \mathrm{Tr}(j,i) \tag{20}$$

It is introduced in Equation 15 allowing to get the following expression:

$$\frac{df(i,t)}{dt} = \sum_{j=1}^{n} M(j,i) f(j,t) \tag{21}$$

The master equation is the main tool allowing the temporal variation of a volume fraction to be estimated. This relationship applies at the unit volume scale as well as at the grain scale. Without the presence of heterogeneous residual stress, the grain can be considered as a typical Boltzmann stochastic system. This point is addressed in subsection 2.4 and subsection 2.6.

2.4 Previous modeling

In the modeling proposed by [26], β_s is considered to be a constant (temperature independent). Moreover, it is assumed that the Boltzmann system is always at the thermodynamic equilibrium so that we get at the grain scale:

$$\frac{df_g(i,t)}{dt} = 0, \ \forall i = 1, \cdots, n \tag{22}$$

When the Boltzmann system is at equilibrium, it is by nature extensive, meaning that N standard units possess the exact same variant volume fractions as 1 standard unit (Equation 23 and Equation 24). At the equilibrium state, for the system containing 1 standard unit, the volume fraction of each variant $f(i,t)$ equals the probability of presence for variant i, $\mathrm{prob}(i,t)$, whereas the Boltzmann distribution is the unique and converged solution of (Equation 25).

$$f_g(i,t) = f_{N=1}(i,t), \ \forall i = 1, \cdots, n \tag{23}$$
$$\frac{df_g(i,t)}{dt} = \frac{df_{N=1}(i,t)}{dt} = 0, \ \forall i = 1, \cdots, n \tag{24}$$
$$f_{N=1}(i,t) = N\,\mathrm{prob}(i,t) = \mathrm{prob}(i,t) = \frac{\exp(-\beta_s \mathfrak{g}(i,t))}{\sum_{j=1}^{n} \exp(-\beta_s \mathfrak{g}(j,t))} \tag{25}$$

Despite these strong hypotheses, a pretty good prediction of the transformation threshold of Ni-Ti SMA alloy under multiaxial stress condition was obtained; a good qualitative estimation of phase composition under thermal loading was obtained too [27][13]. However, due to the thermodynamic equilibrium assumption, the thermomechanical behavior is reversible. An artificial germination energy barrier had to be introduced to produce a major hysteresis loop (partial loops were not modeled). The master equation can provide a more natural modeling of hysteresis when the Boltzmann system is considered out of equilibrium.

2.5 Out-of-equilibrium phase transformation

Herein, we focus on the Boltzmann system containing 1 standard unit ($N = 1$). A generalization towards Boltzmann system at grain scale consisting of N standard units is addressed in subsection 2.6. Hysteresis phenomena are the macroscopic outcomes of time evolution for out-of-equilibrium microscopic systems, indicating that :

$$\frac{df(i,t)}{dt} \neq 0, \forall i \in [1, \cdots, n] \tag{26}$$

c_{ij} constants are consequently bounded:

$$0 \leq c_{ij} \leq \infty, \ \forall (i,j) \ i \neq j \tag{27}$$

In order to highlight the source of hysteresis when the system is out of equilibrium, the classic notion of meta-stable and associated transition probability have to be introduced.

2.5.1 Meta-stable and Transition probability

We seek to compare the Gibbs free energy density of three chosen variants i, j and k. Their Gibbs free energy density is supposed given by the function plotted in Figure 2: variant i exhibits the lowest energy that corresponds to a 'stable' state; variant k has the highest Gibbs free energy that corresponds to an 'unstable' state; The intermediate variant j exhibits an intermediate energy level in a local minimum that corresponds to a 'metastable' state.

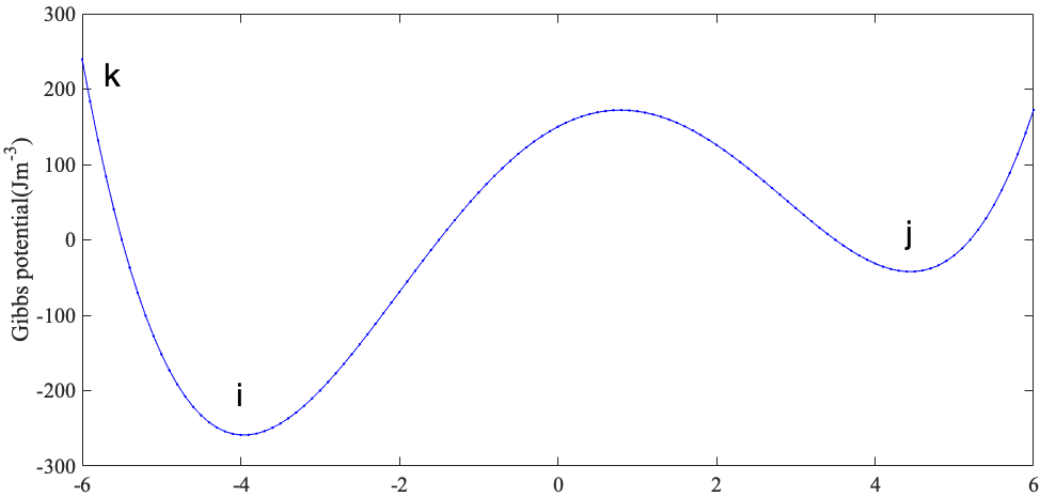

Figure 2: Schematic evolution of Gibbs free energy density in variant space (seen as a continuous function): illustration of unstable(k), stable(i) and metastable(j) variants.

The transition probability matrix $\mathrm{Tr}(i,j)$ helps us to define these different states in a stochastic way. Indeed, we have:

$$\mathrm{Tr}(i,j) = \mathrm{Tr}(i,k) = 0 \tag{28}$$

$$\mathrm{Tr}(k,i) = 1 \tag{29}$$

$$\mathrm{Tr}(j,i) = c_{ji}\exp(-\beta_s(g(i,t) - g(j,t)) \tag{30}$$

Equation 28 indicates that the transition probability for variant i to transform towards other variant is strictly 0. This state corresponds to the stable state and applies to variant i in Figure 2. On the contrary, when the variant k is unstable, the transition probability for variant k to transform towards stable variant i is strictly 1. Equation 29 illustrates this situation. Equation 30 applies for the metastable situation. Indeed, variant j *may* transform to variant i: the transition probability for variant j to transform towards stable variant i is consequently a constant between $[0,1]$.

2.5.2 Metastable and Germination energy density

A metastable variant j can transform towards a stable variant i at time $t' = t + dt$ once it affords an additional energy $d\mathfrak{g}(j,i,dt)$ to ensure that the transition probability equals to one.

$$\mathfrak{g}(j,t) \geq \mathfrak{g}(i,t) + d\mathfrak{g}(j,i,dt) \rightarrow \mathrm{Tr}(j,i) = 1 \tag{31}$$

This additional energy term can be divided into two parts(see Equation 32):

- $d\mathfrak{g}^c(dt)$: this term is the meta stable germination energy density, it decreases as function of time dt (see Equation 33 and Equation 34)
- $d\mathfrak{g}^a(j,i)$: this term is the mechanical incompatibility related germination energy density between variant i and j (a same kind of germination energy associated with mechanical incompatibility has been proposed in [35] and [30])

$$d\mathfrak{g}(j,i,dt) = d\mathfrak{g}^c(dt) + d\mathfrak{g}^a(j,i) \tag{32}$$

$$d\mathfrak{g}^c(dt=0) = -\frac{\log(c_\mu)}{\beta_s} \tag{33}$$

$$d\mathfrak{g}^c(dt=\infty) = 0 \tag{34}$$

2.5.3 Saturation of hysteresis loop and temporal relaxation of germination energy

In stochastic theory, when the variation of Gibbs free energy density from variant j to variant i is overwhelmingly higher than the corresponding germination energy density, the transformation takes place immediately without any temporal delay. This transformation generates an incompressible energy loss associated to the predefined difference of Gibbs free energy between the two variants. In other words, for this type of configuration, the hysteresis loop is always saturated and remains constant (see Equation 33), ignoring any possible dynamic effect.

Otherwise, when the variation of Gibbs free energy density from variant j to variant i is not high enough to achieve the immediate transformation, the accumulation of transition probability with an increasing differential time interval $p_{acc}(j \to i, t' = t + dt)$, would allow the transition to eventually occur. A time delay is consequently necessary to achieve the transformation. The associated energy loss is on the other hand lower in accordance with a lower Gibbs free energy difference, which is only related to the mechanical incompatibility between variants (see Equation 35 and Equation 36).

When an infinite time is considered and mechanical incompatibilities are neglected $d\mathfrak{g}^a(i,j) = 0, \forall (i,j)$, the system does not have theoretically to compensate any germination energy $d\mathfrak{g}(j,i)$ in order to achieve the transformation (see Equation 36). Consequently the Boltzmann system can reach its equilibrium state leading to a reversible behavior (see Equation 37 and Equation 36). This point has been already addressed in subsection 2.4.

$$p_{acc}(j \to i, t' = t + dt) = \int_t^{t+dt} \mathrm{Tr}(j,i)dt \tag{35}$$

$$d\mathfrak{g}(j,i,dt = \infty) = 0 + d\mathfrak{g}^a(j,i) = 0 \tag{36}$$

$$p_{acc}(j \to i, t' = \infty) = \int_t^{\infty} \mathrm{Tr}(j,i)dt = 1 \tag{37}$$

2.6 Numerical difficulties

When the Boltzmann system contains only 1 or a few of standard units, the temporal evolution of the volume fraction of each variant can be analytically calculated from the implemented germination energy barrier. However, at the grain scale, when the Boltzmann system (grain) consists of N standard units, the system is associated with n^N different levels of Gibbs free energy. To give a short example, for the grain at configuration ξ, which consists of N standard units (SU), and N_i is the sub-population of standard unit described by each variant i. The associated energy level can be expressed as :

$$\xi = [N_1, N_2, \cdots N_n], \text{ with } \sum_{i=1}^{n} N_i = N = \sum_{i=1} \xi(i) \tag{38}$$

$$\mathfrak{g}_g(\xi, t) = \frac{1}{N} \sum_{i=1}^{n} N_{_i}(t)\mathfrak{g}_i(t) \tag{39}$$

The average Gibbs free energy density associated to configuration ξ, should be seen as probabilistic quantity where all linear combinations (n^N combinations in total) should be tested to extract the *grand* probability function (i.e. the highest probability at infinite time instant $f_g(i, t = \infty)$ corresponding to the combination where the average Gibbs energy density at the grain scale is minimized).

The master equation and volume fraction for variant i at grain scale can be written, considering two different possible configurations $\{\xi, \xi^*\}$:

$$\frac{d\hat{f}(\xi,t)}{dt} = \sum_{\xi^*=1}^{n^N} M(\xi,\xi^*)\,\hat{f}(\xi^*,t) \tag{40}$$

$$f_g(i,t) = \sum_{\xi=1}^{n^N} \hat{f}(\xi,t)\frac{\xi(i)}{N} \tag{41}$$

where $\hat{f}(\xi, t)$ is the volume fraction of configuration ξ at time instant t.

The computation cost of the master equation may grow very fast with an increasing number of SU required to get a stochastic result. Classical procedures are consequently not relevant to solve the problem analytically. An alternative way is proposed, detailed in the next section.

3 Kinetic Monte-Carlo framework at the grain scale

The use of Kinetic Monte-Carlo (KMC) algorithm can be traced back to the early work of [4] and [10]. This algorithm is essentially a re-organization of former stochastic algorithms. By deploying the density of transformation probability function, it accounts for the previous distribution of volume fractions and the state of Markov Transition Matrix (both at time instant t), to get the volume fractions at the next investigated time instant t'. Doing this way, we aim to evaluate the current state of the master equation at the given time t instead of solving analytically the master equation itself. Based on these indirect observations, the temporal volume fraction variation is generated through the KMC framework in a stochastic way. After a sufficient number of repeated samplings, the stochastic average should converge towards the analytic response of the master equation at the grain scale.

3.1 Transformation quantities and transformation weight

We first consider the initial time instant $t = t_0$. An initial volume fraction of variant i $f(i, t_0)$ inside the grain can be defined at this time instant. Equation 42 gives the raw increase and decrease of the volume fraction of variant i:

$$\frac{df(i,t)}{dt} = \sum_{j=1}^{n} M(j,i) f(j, t = t_0) \tag{42}$$

or

$$\frac{df(i,t)}{dt} = \frac{df_b(i,t)}{dt} + \frac{df_d(i,t)}{dt} \tag{43}$$

The raw transformation birth quantities $\zeta(t = t_0)$ are given by:

$$\zeta(t = t_0) = N \sum_{i=1}^{n} \frac{df_b(i,t)}{dt} \tag{44}$$

ζ evaluates the total number of variants transformed inside the Boltzmann system at instant $t = t_0$.
We seek next to obtain the weight of each transformation type inside ζ. Therefore $\gamma(j, i, t = t_0)$ in Equation 45 indicates the weight of transformation from $j \to i$ inside the total transformed quantities ζ at instant $t = t_0$.

$$\gamma(j, i, t = t_0) = N \frac{M(j,i) f(j, t = t_0)}{\zeta(t = t_0)} \tag{45}$$

$\zeta(t = t_0)$ and $\gamma(j, i, t = t_0)$ describe the global tendency of the master equation at instant $t = t_0$. These quantities indirectly indicate when the next transformation triggers and which variant is chosen to transform towards another variant in the Boltzmann system. These parameters can be denoted as the 'indirect observers' of the Boltzmann system. To describe directly the evolution of the volume fraction, two new concepts must be introduced: the first transformation time τ and the first transformation type μ.

3.2 First transformation time and first transformation type

First transformation time and *first transformation type* are two variables defining the stochastic Monte-Carlo step (τ, μ).

- τ is the first transformation time. It corresponds to the time delay needed for at least a SU inside the system to transform from one variant to another for the time instant $t = t_0$.
- $\mu : j \to i$ is the first transformation type. It is evaluated when at least one SU is transformed. A μ type transformation is corresponding to a specific transformation of variant j towards variant i (since $i \neq j$, there are $n^2 - n$ possible transformation types).

Parameters (τ, μ) describe exactly the time delay for the first transformation and the associated transformation type.

Given the indirect observers of the Boltzmann system (ζ, γ), the transition probability to have a (τ, μ) transformation can be written following (mathematical demonstration available in [10]):

$$p(\tau, \mu) d\tau = \gamma(\mu, t) \exp(-\zeta(t)\tau) \tag{46}$$

$$\gamma(\mu, t) = \gamma(j, i, t), \forall (i, j), i \neq j \tag{47}$$

where $p(\tau,\mu)d\tau$ indicates the probability at time t that a SU transforms in the time interval $[t+\tau, t+\tau+d\tau]$ inside a Boltzmann system consisting of N SU, and that this transformation is a μ type transformation.
For the sake of simplicity, Equation 47 is introduced and used throughout this paper[2].

3.3 Procedure for random generation of (τ,μ)

As mentioned in the previous section, (τ,μ) are the two direct stochastic descriptors for the hysteretic behavior at the grain scale. The classical approach to generate a pair of variables based on the probability function is referred as 'conditioning': $p(\tau,\mu)$ can be built through the product of two independent one-variable density of probability functions $p_1(\tau)$ and $p_2(\mu|\tau)$, where $p_1(\tau)$ and $p_2(\mu|\tau)$ indicate the probabilities of two cause-related events:

1. $p_1(\tau)$ measures whether or not at least one variant inside the system transforms into a different variant type in the differential time interval $[t, t+\tau]$.

2. $p_2(\mu|\tau)$ is the conditional probability measuring when at least one variant inside the system transforms into a different variant type in the differential time interval $[t, t+\tau]$ following a μ type transformation.

These conditional probability functions can be estimated using the current transformation quantity $\zeta(t)$ and the associated transformation weight $\gamma(\mu,t)$ following:

$$p(\tau,\mu) = \gamma(\mu,t)\exp(-\zeta(t)\tau) = p_1(\tau)p_2(\mu|\tau) \tag{48}$$

$$p_1(\tau) = \sum_{\mu} p(\tau,\mu) = \exp(-\zeta(t)\tau)\zeta(t) \tag{49}$$

$$p_2(\mu|\tau) = \frac{\gamma(\mu,t)}{\zeta(t)} \tag{50}$$

In the work of [10], it is demonstrated that the generation of τ and μ can be done separately based on $p_1(\tau)$ and $p_2(\mu|\tau)$ (see Equation 49 and Equation 50). The numerical implementation of random number generations (RNG) to produce (τ,μ) by using Inverse Monte Carlo technique is discussed in Appendix B.

3.4 Kinetic Monte-Carlo framework

The basic idea of this computation procedure is to deploy the two-variables density of probability function $p(\tau,\mu)$ using a Monte-Carlo technique to generate the two stochastic descriptors (τ,μ) of the system at current time t. To begin with, we simplify the problem by neglecting the heat emission (absorption or emission) impact due to the phase transformation. With this simplification, the Kinetic Monte-Carlo algorithm at the grain scale is straightforward and can be summarized as follows (the corresponding KMC algorithm flowchart for a grain is shown in Appendix A):

Step 0: Set the time variable t at t_0. Define the total variant population N inside the grain system and initialize the volume fraction for each variant $f(i,t_0), i=1,\cdots n$; specify c_{ji} according to each type of transformation $\mu \to (j,i)$; specify a series of *sampling time* and a stopping time: $t = t_1 < t_2 \cdots < t_n < \cdots t_{stop}$ with a time interval dt between each sampling time step; reposition t in the differential time interval $[t_{n-1}, t_n]$; load the crystal texture then interpolate the Gibbs free energy density $\mathfrak{g}(i,t), i=1,\cdots n$ for each variant at current time t in each grain;

Step 1: Using Equation 15, calculate $\zeta(t)$ and $\gamma(\mu,t)$ which collectively determine the density of transformation probability function $p(\tau,\mu)$ in Equation 46; select a proper inverse Monte Carlo technique to generate one random pair (τ,μ) based on the joint density probability function $p(\tau,\mu)$ pre-calculated at the previous step; an explicit random variable generation technique is used for this step: it is detailed in Appendix B.

Step 2: Deploy the two random variables (τ,μ) obtained at the previous step; increment the current time t by τ; update the variant population involved in transformation $\mu : j \to i$.

[2] We reshape a matrix towards a vector by this numerical operation.

$$
\begin{aligned}
&t' = t + \tau \text{ and } dt = \tau \\
&df(\mu, t) = M(j, i) f(j, t) \tau \\
&f(i, t') = f(i, t) + df(\mu, t) \\
&f(j, t') = f(j, t) - df(\mu, t) \\
&t = t'
\end{aligned} \tag{51}
$$

.

Step 3: If τ is higher than the sampling time interval $[t_m, t_{m+1}]$, increment t towards t_{m+1} keeping the volume fractions unchanged; if $t > t_{stop}$, return to Step 0 , otherwise return to Step 1.

Step 4: Perform N_s independent Kinetic Monte-Carlo repeated samplings; obtain the stochastic average response for grain g.

Concerning the last point, indeed, when a complex thermomechanical loading is applied, several variants may have the same level of Gibbs free energy at current time t, meaning that the activation of these transformation types are equiprobable. The KMC procedure will randomly choose a specific transformation type and move forward based on the probability functions, leading to a final result that may have been different if another transformation type had been chosen. The solution is to multiply KMC estimations $f_d(i,t)$ and process to a stochastic average $f_{st}(i,t)$ as defined in Equation 52. The result converges to the macroscopic solution $f_{sol}(i,t)$ when enough independent KMC samplings are performed.

$$
f_{st}(i,t) = \lim_{N_s \to \infty} \frac{1}{N_s} \sum_{d=1}^{N_s} f_d(i,t) = f_{sol}(i,t) \tag{52}
$$

An exact convergence criterium of the Monte-Carlo process cannot however be properly estimated (mentioned as stochastic fluctuation). The most discriminant situation is probably the simulation of a pure thermal loading (DSC scan for example), because all variants are equiprobable at the transformation temperature. The simulation requires several independent samplings before the convergence is suitably reached (see next section and Figure 25).

3.5 Kinetic Monte-Carlo framework with additional heat source due to a phase transformation

Heat emission or absorption are not considered in the previous sections. It is however possible to evaluate their effects by solving the heat equation and by using admissible boundary conditions to mimic the anisothermal behavior. The heat equation that can apply in the framework of a stochastic approach considering a $\mu : i \to j$ transformation at time instant τ is given by:

$$
dT(\tau, \mu) = \frac{1}{\rho c_p} L_{ij} df(\tau, \mu) + \frac{\tau}{\rho c_p} \kappa \Delta_L(T) \tag{53}
$$

This form that neglects the thermoelastic heat source is demonstrated in Appendix D. It involves the latent heat associated with $\mu : i \to j$ transformation which writes:

$$
L_{ij} = h_i - h_j - \boldsymbol{\sigma} : (\boldsymbol{\epsilon}_i^{tr} - \boldsymbol{\epsilon}_i^{tr}) \tag{54}
$$

Using Equation 53, an adiabatic situation can easily be modeled by neglecting the thermal diffusion. Of course any spatial derivation has no direct physical signification for modeling at RVE scale. An anisothermal situation, intermediate between adiabatic and isothermal extreme situations can only be modeled by transforming the Laplacian by an equivalent convection effect, supposing that the RVE is embedded in a coolant. Heat conduction term in Equation 53 is then replaced by:

$$
\kappa \Delta_L(T) \to k(T - T_{amb}) \tag{55}
$$

where T_{amb} is the ambient temperature, T is the temperature of the medium and k an equivalent convection coefficient. We can consider the following situations:

- $k = 0$: the system is adiabatic, without heat exchange with environment;
- $k = \infty$: ideal convection: the temperature is fully controlled by the ambient temperature, leading to the isothermal situation;

- $\infty \geq k \geq 0$: intermediate anisothermal situations

By solving Equation 53, we can calculate the temperature variation $dT(\tau, \mu)$ at each time step.

$$\begin{aligned} t' &= t + \tau \\ T(t') &= T(t) + dT(\tau, \mu) \\ t &= t' \end{aligned} \tag{56}$$

In the present paper, no real convergence between KMC and heat equation has been looked for to avoid too long computation time. One alternative strategy is to update the temperature at each time step and consider it for the next calculation. A converged result is not guaranteed but the chosen time interval $[t_n, t_{n+1}]$ is sufficiently small to describe the evolution of temperature with a good accuracy and observe some relevant anisothermal effects.

3.6 Homogenization and localization

The procedure has been detailed for a grain g in the previous sections but it can apply the same way for all grains of RVE (polycrystal defined by the Orientation Data Function - ODF - obtained via Electron Back-Scattered Diffraction - EBSD - measurement). Once $f(i,t)$ is defined, the calculation of average transformation strain $\boldsymbol{\epsilon}_{tr}(g)$ and entropy density $s(g)$ (as associated variables to stress and temperature loading) over the grains is easily obtained:

$$\boldsymbol{\epsilon}_{tr}(g) = \sum_{i=1}^{n} f(i)\boldsymbol{\epsilon}_{tr}(i) \tag{57}$$

$$s(g) = \sum_{i=1}^{n} f(i)s(i) \tag{58}$$

The same quantities can be calculated at the RVE scale by averaging over the grains. It must be noticed that no strain localization is required since homogeneous stress assumption[13] is retained for all calculations.

$$\boldsymbol{\epsilon}_{tr} = \frac{1}{N_g} \sum_{g=1}^{N_g} \boldsymbol{\epsilon}_{tr}(g) \tag{59}$$

$$s = \frac{1}{N_g} \sum_{g=1}^{N_g} s(g) \tag{60}$$

Total deformation (sum of elastic, thermal and transformation) can be built by a simple summation of quantities whatever the scale.
Application of localization procedures is possible from RVE to grain scales. This localization is for example required if a real single crystal stiffness tensor (usually anisotropic) is considered for the polycrystalline calculation. Different localization procedures can however be applied. The most relevant is probably the self-consistent that allows the stress at grain scale $\boldsymbol{\sigma}_g$ to be defined as function of the applied macroscopic stress $\boldsymbol{\sigma}$, the transformation deformation matrix at the grain and macro scales, the accommodation stiffness tensor $\mathbb{C}^{acc}$ and the stress concentration tensor $\mathbb{B}$ (see more details concerning this procedure in [9]).

$$\boldsymbol{\sigma}(g) = \mathbb{B}(g) : \boldsymbol{\sigma} + \mathbb{C}^{acc}(g) : (\boldsymbol{\epsilon}_{tr} - \boldsymbol{\epsilon}_{tr}(g)) \tag{61}$$

Once the full knowledge of transformation strain for each grain is given, the macroscopic response $\boldsymbol{\epsilon}_{tr}$ of the material is obtained, through an averaging operation involving a strain localization:

$$\boldsymbol{\epsilon}_{\mathrm{tr}} = \frac{1}{N_{\mathrm{g}}} \sum_{\mathrm{g}=1}^{N_{\mathrm{g}}} {}^{t}\mathbb{B}(\mathrm{g}) : \boldsymbol{\epsilon}_{\mathrm{tr}}(\mathrm{g}) \tag{62}$$

4 Identification procedure of the modeling parameters

A $\mathrm{Ni}-50.2\mathrm{Ti}$ SMA is chosen to illustrate the identification procedure. The Ni-Ti SMA has been heat treated at $T = 773K$ for 1 hour and quenched in cold water. The parameters used in the model include:

- Chemical and thermal properties;

- Mechanical properties;
- Crystalline properties and texture;
- Instant germination energy.

4.1 Chemical and thermal properties

The Differential Scanning Calorimetry (DSC), consists in measuring the difference in heat flux between a specimen and a reference (often an empty crucible) at stress free state, and aims to determine the chemical properties of the material:

- Specific heat capacity c_p ;
- Phase transformation properties, including transition temperatures T_{tr}, associated latent heat densities δh and variations of entropy s and enthalpy h densities.

The DSC analysis is conducted over a small sample (8.4 mg) taken from a virgin specimen of NiTi SMA. A quasi-static thermal cycle is applied:

- Isothermal at $T = 373K$ for 10 min;
- Cooling from $T = 373K$ to $T = 193K$ with a temperature rate of $\dot{T} = 5\,\mathrm{K\,min^{-1}}$;
- Isothermal at $T = 193K$ for 10 min;
- Heating from $T = 193K$ to $T = 373K$ with a temperature rate of $\dot{T} = 10\,\mathrm{K\,min^{-1}}$;

This cycle is usually repeated two times.

Thermal hysteresis and phases.
The DSC measurement used for the identification is plotted in Figure 3. It confirms that for the investigated NiTi SMA, three principal phases may exist depending on the temperature: austenite (A), martensite (M) and *so-called* R-phase. Two significant heat flux peaks are observed during the cooling stage. They correspond to the A→R and R→M phase transformations. Only one significant heat flux peak is observed during the heating stage. It may be possible that the backward transformation M→A passes through the intermittent formation of the R phase.

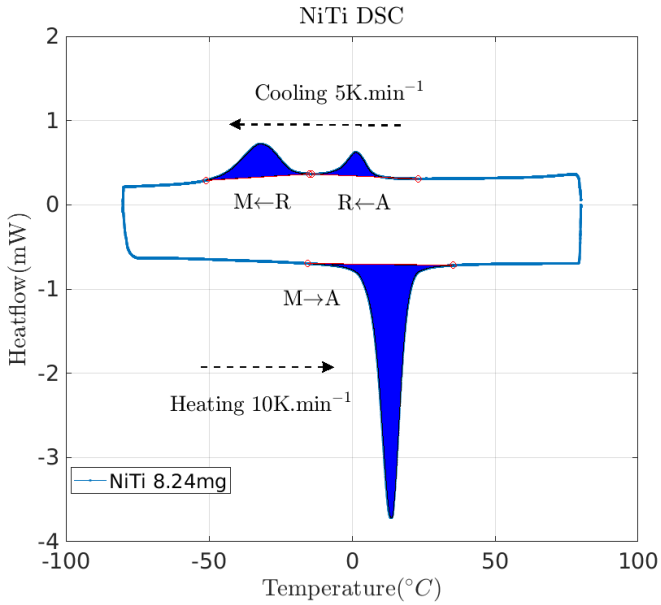

Figure 3: DSC: Heat flow as function of temperature

Specific heat capacity.

In the area without phase transformation, the difference measured in heat flux between the specimen and a reference crucible can be interpreted as the heat required by the material to maintain the temperature variations, which helps us to identify the specific heat capacity of the specimen. The following relationships apply:

$$\begin{aligned} p &= \rho c_p \dot{T} \\ c_p &= \frac{p}{\rho \dot{T}} \end{aligned} \tag{63}$$

where p represents the heat flow difference without phase transformation and ρ is the mass density.

The specific heat capacity of A, R and M phases in NiTi SMA are nearly close. For simplicity reasons, we will assume for calculations that the three phases share the same specific heat capacity:

$$c_p^A = c_p^M = c_p^R = c_p \tag{64}$$

Latent heat.

Latent heat (or enthalpy of transition) is defined as an additional quantity of heat exchanged between the external heat source and the analyzed specimen to maintain the same reference command temperature during the phase transformation. Herein the raw curve[3] of heat flux as function of time during cooling is used to explain the protocol.

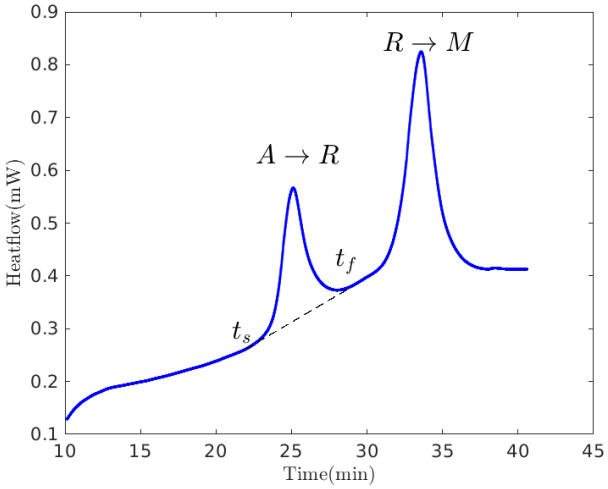

Figure 4: Determination of latent heat Δh: example of NiTi SMA during DSC (cooling).

As illustrated in Figure 4, by defining the transformation start and finish time (or temperature), the specific latent heat Δh can be calculated as follows:

$$\Delta h = \frac{1}{V} \int_{t_s}^{t_f} p(t) dt \tag{65}$$

where $p(t)$ represents the additional heat flux (mW) required by the specimen to ensure the phase transformation. V is the volume of material used for the DSC.

Transformation temperature and variation of entropy.

Usually, the transformation temperature is defined at the point where the additional heat flux reaches its maximum during the DSC measurement. As shown in Figure 5, T_1 represents the transformation temperature during the cooling from A $\rightarrow$ R and T_2 represents the transformation temperature during the cooling from R $\rightarrow$ M. Given these temperatures, the variation in entropy density can be expressed as follows (T_{tr} figures out T_1 or T_2):

$$\Delta s = \frac{\Delta h}{T_{tr}} \tag{66}$$

As for enthalpy density, only the variation of entropy density is relevant for the modeling. Table 1 gathers the different modeling parameters extracted from the DSC experiment.

[3] before baseline correction

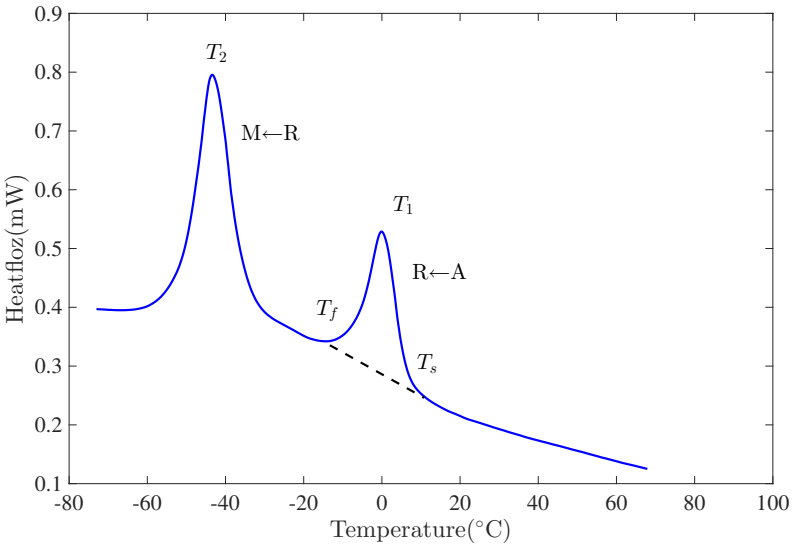

Figure 5: Transformation temperature and entropy variations: example of NiTi SMA during DSC (cooling).

Parameters	Symbol	Value
Specific heat capacity	$c_p\,[\mathrm{J\,kg^{-1}\,K^{-1}}]$	460 ± 20
Latent heat density $A \to R$	$\Delta h(A \to R)\,[\mathrm{MJ\,m^{-3}}]$	40 ± 4
Latent heat density $R \to M$	$\Delta h(A \to M)\,[\mathrm{MJ\,m^{-3}}]$	98 ± 6
Variation of entropy density $A \to R$	$\Delta s(A \to R)\,[\mathrm{MJ\,m^{-3}\,K^{-1}}]$	0.14 ± 0.02
Variation of entropy density $R \to M$	$\Delta s(A \to M)\,[\mathrm{MJ\,m^{-3}\,K^{-1}}]$	0.38 ± 0.02

Table 1: NiTi SMA chemical parameters identified by DSC

469

4.2 Mechanical properties

The mechanical properties that are looked for are mainly the elastic properties. Considering the material as isotropic, only the Young modulus and Poisson ratio must be identified. We use for that purpose the results of a more complete study addressing the pseudo-elastic behavior of the NiTi SMA subjected to a uniaxial loading and a concomitant identification of the phases produced during the strengthening [6]. Since the phase transformation occurs through localization bands, a measurement of the kinematic fields by digital image correlation (*PGD-RT3* DIC code developed by LMT) is necessary (see the work of [2] for more details about the DIC code). The same tool can be used to extract the elastic properties.

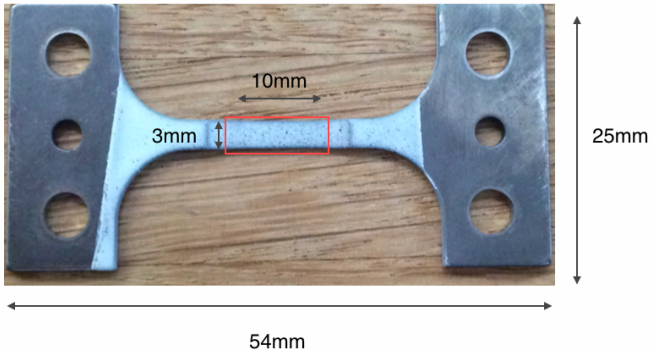

Figure 6: 1D strip specimen with black and white speckle paints; $10 \times 3\,\mathrm{mm}^2$ surface used for DIC measurement is highlighted.

Figure 6 shows the sample used for the experiment. The central region used for DIC is a parallelepipedic volume, *i.e.* $10 \times 3 \times 0.3\mathrm{mm}^3$. Longitudinal and transversal average deformations have been extracted at several stress levels. The engineering stress expresses as follows:

$$\sigma_{xx} = \frac{F}{S_0} \tag{67}$$

where F is the axial force recorded by the force cell of the loading machine and S_0 is the initial section of the NiTi strip. We can for example build a *virtual strain gauge* to extract the averaged axial and transversal strain over the chosen area S of the image:

$$\epsilon_{xx} = \frac{1}{S} \iint_S \tilde{\epsilon}_{xx}(x,y)\, dxdy \tag{68}$$

$$\epsilon_{yy} = \frac{1}{S} \iint_S \tilde{\epsilon}_{yy}(x,y)\, dxdy \tag{69}$$

The longitudinal and transversal averaged stress-strain curves are plotted in Figure 7. The basic elastic properties (Young modulus and Poisson ratio) can be easily calculated. Values are reported in Table 2. For simplicity reasons, elastic properties will be considered identical for all phases.

$$\begin{aligned} E_Y &= \frac{\sigma_{xx}}{\epsilon_{xx}} \\ \nu &= -\frac{\epsilon_{yy}}{\epsilon_{xx}} \end{aligned} \tag{70}$$

Parameters	Symbol	Value
Young modulus	E_Y [GPa]	60 ± 9
Poisson ratio	ν	0.31 ± 0.02

Table 2: Elastic parameters identified by 1D tensile testing

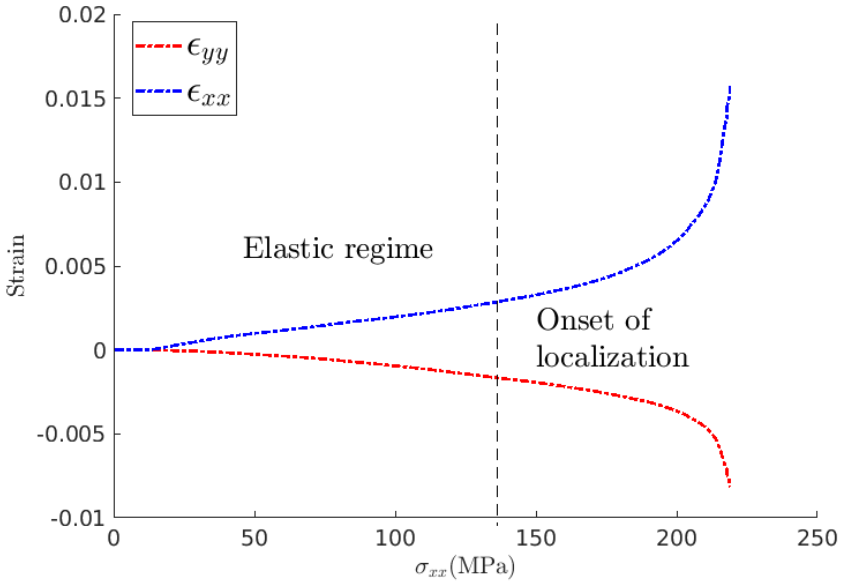

Figure 7: Longitudinal strain ϵ_{xx} and transversal strain ϵ_{yy} as function of engineering stress σ_{xx} for 1D NiTi SMA strip

The dilatation coefficient is a thermo-mechanical parameter. Its identification via a dilatometer set-up is not a problem. However, it has not been identified since dilatation effects have not been considered in the modeling (α_v set at $0\,\mathrm{K}^{-1}$). Indeed associated deformations are negligible comparing to elastic or transformation strains for the temperature range addressed in this work. The mass density $\rho = 6450\,\mathrm{kg\,m}^{-3}$ (in accordance with literature) has been estimated using a dedicated balance (see Table 3 for these two more parameters).

Parameters	Symbol	Value
Dilatation coefficient	α_v $[\mathrm{K}^{-1}]$	not meas.
Mass density	ρ $[\mathrm{kg\,m}^{-3}]$	6450 ± 160

Table 3: Dilatation coefficient and mass density.

4.3 Crystalline parameters and texture identification

As already mentioned, A, M and R-phase may exist in the material depending on thermal and stress conditions. Austenite is a cubic phase denoted as *parent phase* that exhibits only one variant numbered $i = 17$. The R-phase is rhombohedral and exhibits 4 variants numbered from $i = 13$ to $i = 16$. Martensite is a monoclinic phase exhibiting 12 variants numbered from i=1 to i=12. An identification of the crystalline parameters of these phases is possible by a measurement of X-ray diffraction spectrum carried out under stress at room temperature.

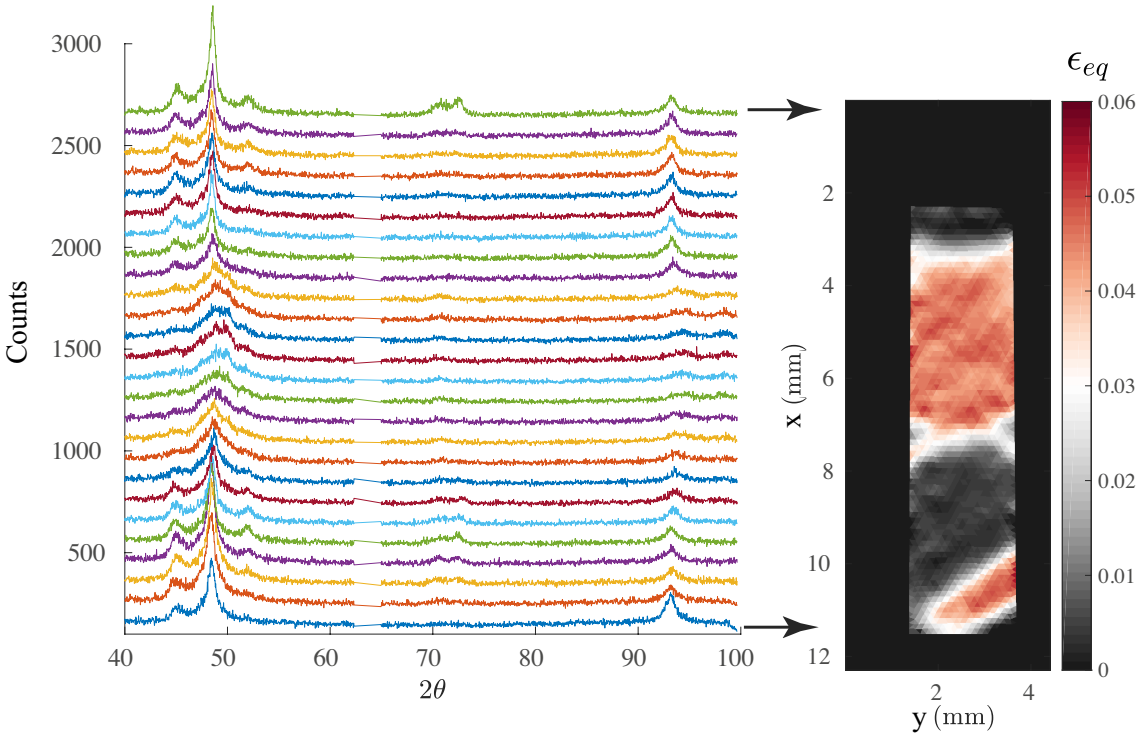

Figure 8: X-ray diffraction spectrum field measured at different position along the tensile specimen and associated von Mises equivalent strain field.

Indeed, the mechanical test presented in the previous section can be led to deformations levels where the martensitic phase transformation occurs. Figure 8 right thus plots the spatial evolution of the von Mises equivalent strain. This result shows that the transformation takes place in a heterogeneous way in the form of localization bands (they can be multiple [11]). A simultaneous measurement of the spatial evolution of the X-ray spectrum has been carried out (see [6] for more details about the procedure). The different spectra are presented in Figure 8 left, highlighting that A/M/R phases do coexist in the sample. A dedicated procedure [6] allows on the other hand the typical experimental spectrum of the three phases to be plotted (Figure 9). The indexation of diffraction patterns can be achieved by using the Bragg's law:

$$\frac{n\lambda}{2d_{hkl}} = \sin(\theta_{hkl}) \tag{71}$$

where d_{hkl} denotes as the inter-planar spacing between two (hkl) planes and λ is the wavelength of X-ray radiation source. The theoretical values for the inter-planar spacing of A/M/R phases for the equiatomic NiTi SMA are given as function of the lattice parameters (see the work of [8]) by:

$$d_{hkl} = \frac{a_0}{\sqrt{h^2 + k^2 + l^2}} \rightarrow \text{A phase} \tag{72}$$

$$d_{hkl} = \frac{a_R\sqrt{1 - 3\cos^2(\alpha) + 2\cos^3(\alpha)}}{\sqrt{(h^2 + k^2 + l^2)\sin^2(\alpha) + 2(hk + kl + hl)(\cos^2(\alpha) - \cos(\alpha))}} \rightarrow \text{R phase} \tag{73}$$

$$d_{hkl} = \frac{\sin(\beta)}{\sqrt{\dfrac{h^2}{a_M^2} + \dfrac{k^2\sin^2(\beta)}{b_M^2} + \dfrac{l^2}{c_M^2} - \dfrac{2hl\cos(\beta)}{a_M c_M}}} \rightarrow \text{M phase} \tag{74}$$

The theoretical spectra have been plotted in Figure 10. By a parameter optimization of the theoretical patterns to fit the experimental patterns, it is possible to identify the lattice

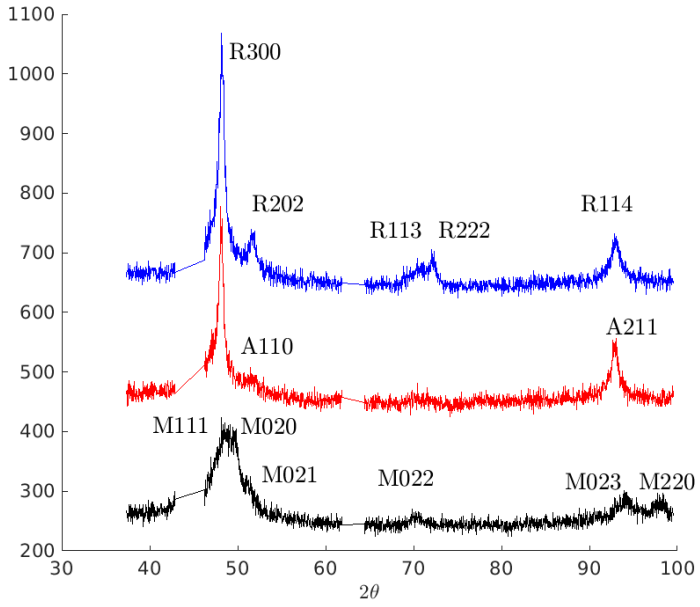

Figure 9: Three diffraction scans of Ni-Ti SMA indexed using the diffraction theory, showing: R-phase (in blue), austenite (in red), and martensite (in black) - representation using a vertical offset of 200 counts between each spectrum.

parameters after removal of stress effect (shift of peaks associated with elastic deformation). Errors obtained are however too large to make a relevant identification. It has been consequently decided to use parameters from literature, in good agreement with our experimental observations [39][17]. Lattice parameters are (errors are not given, defined by the last significant number):

- Austenite: $a_0 = 0.3015\,\text{nm}$;
- R-phase: $a_R = a_0 = 0.3015\,\text{nm}$; $\alpha = 91.5°$;
- Martensite: $a_M = 0.2889\,\text{nm}$; $b_M = 0.4120\,\text{nm}$; $c_M = 0.4622\,\text{nm}$; $\beta = 96.8°$.

The associated Bain matrix $\mathbb{U}$ can be constructed as follows Table 4 and Table 5 : (R-Phase - $\eta = 0.998$ and $\delta = -0.0131$; M phase - $\alpha = 1.0243$, $\gamma = 0.9563$, $\delta = 0.058$, $\epsilon = -0.0427$) .

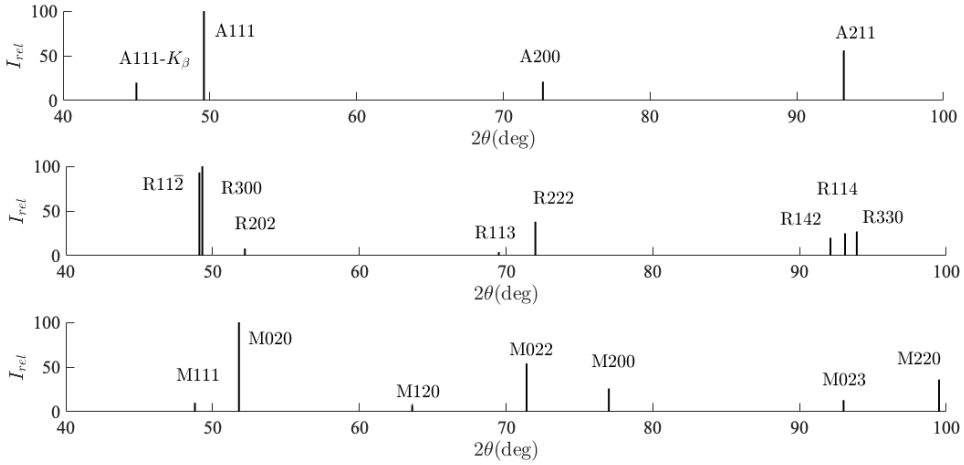

Figure 10: Theoretical diffraction patterns for A, M, and R phases

Austenite has the highest crystal symmetry, the associated Bain matrix is the Identity matrix:

$$U_{17} = \mathbb{I} \tag{75}$$

$U_{13} = \begin{bmatrix} \eta & \delta & \delta \\ \delta & \eta & \delta \\ \delta & \delta & \eta \end{bmatrix}$	$U_{14} = \begin{bmatrix} \eta & -\delta & -\delta \\ -\delta & \eta & \delta \\ -\delta & \delta & \eta \end{bmatrix}$	$U_{15} = \begin{bmatrix} \eta & \delta & -\delta \\ \delta & \eta & -\delta \\ -\delta & -\delta & \eta \end{bmatrix}$	$U_{16} = \begin{bmatrix} \eta & -\delta & \delta \\ -\delta & \eta & -\delta \\ \delta & -\delta & \eta \end{bmatrix}$

Table 4: Bain matrix of R-phase variants [39]

$U_1 = \begin{bmatrix} \gamma & \epsilon & \epsilon \\ \epsilon & \alpha & \delta \\ \epsilon & \delta & \alpha \end{bmatrix}$	$U_2 = \begin{bmatrix} \gamma & -\epsilon & -\epsilon \\ -\epsilon & \alpha & \delta \\ -\epsilon & \delta & \alpha \end{bmatrix}$	$U_3 = \begin{bmatrix} \gamma & -\epsilon & \epsilon \\ -\epsilon & \alpha & -\delta \\ \epsilon & -\delta & \alpha \end{bmatrix}$	$U_4 = \begin{bmatrix} \gamma & \epsilon & -\epsilon \\ \epsilon & \alpha & -\delta \\ -\epsilon & -\delta & \alpha \end{bmatrix}$
$U_5 = \begin{bmatrix} \alpha & \epsilon & \delta \\ \epsilon & \gamma & \epsilon \\ \delta & \epsilon & \alpha \end{bmatrix}$	$U_6 = \begin{bmatrix} \alpha & -\epsilon & \delta \\ -\epsilon & \gamma & -\epsilon \\ \delta & -\epsilon & \alpha \end{bmatrix}$	$U_7 = \begin{bmatrix} \alpha & -\epsilon & -\delta \\ -\epsilon & \gamma & \epsilon \\ -\delta & \epsilon & \alpha \end{bmatrix}$	$U_8 = \begin{bmatrix} \alpha & \epsilon & -\delta \\ \epsilon & \gamma & -\epsilon \\ -\delta & -\epsilon & \alpha \end{bmatrix}$
$U_9 = \begin{bmatrix} \alpha & \delta & \epsilon \\ \delta & \alpha & \epsilon \\ \epsilon & \epsilon & \gamma \end{bmatrix}$	$U_{10} = \begin{bmatrix} \alpha & \delta & -\epsilon \\ \delta & \alpha & -\epsilon \\ -\epsilon & -\epsilon & \gamma \end{bmatrix}$	$U_{11} = \begin{bmatrix} \alpha & -\delta & \epsilon \\ -\delta & \alpha & -\epsilon \\ \epsilon & -\epsilon & \gamma \end{bmatrix}$	$U_{12} = \begin{bmatrix} \alpha & -\delta & -\epsilon \\ -\delta & \alpha & \epsilon \\ -\epsilon & \epsilon & \gamma \end{bmatrix}$

Table 5: Bain matrix of M phase variants [17]

The transformation strain tensor is obtained for each variant following:

$$\boldsymbol{\epsilon}_i^{tr} \simeq \frac{1}{2}(U_i U_i^T - \mathbb{I}), i = 1, \cdots 17 \tag{76}$$

Crystallographic texture

Observations by Scanning Electron Microscope (SEM) and EBSD analyses have been performed over a surface $S = 1\,\mathrm{mm}^2$ of a NiTi SMA sheet after diamond polishing and electro-polishing. The pole figures and inverse pole figures are reported in Figure 11. They clearly illustrate an isotropic transverse texture with a $\langle 111 \rangle$ pole along the normal direction to the sheet. This texture may result in a quite isotropic behavior for stress-controlled experiments loaded in a direction belonging to the sheet plane.

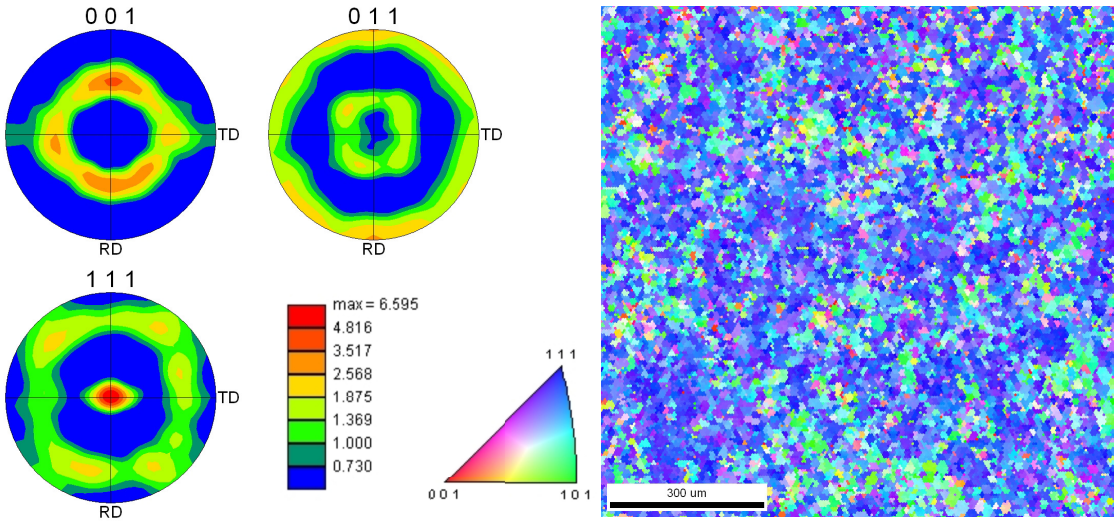

Figure 11: Pole figures and Inverse pole figure (representing orientations normal to the sheet plane) obtained via EBSD.

EBSD analysis also grants to measure the average grain size and grain size distribution. The overall distribution of grain size varies between $8\,\mu\text{m} \leq d \leq 40\,\mu\text{m}$, with an average value of about $d \simeq 15\,\mu\text{m}$. Area defined in Figure 11 right and associated EBSD data can therefore be considered as representative of the material. They define the RVE of the multiscale model introduced in section 2. 413 grain orientations have been selected from the collected crystal FDO as representative of the material texture (see Figure 12) for calculations.

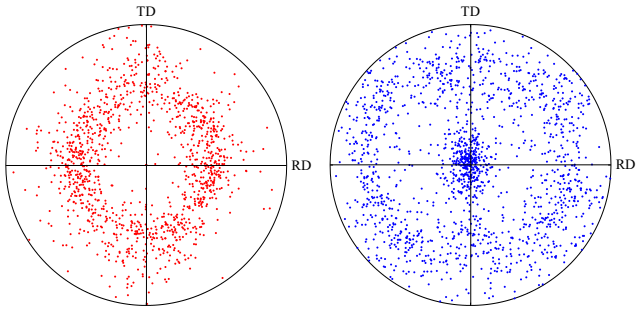

(a) Pole figure $\langle 100 \rangle$ (b) Pole figure $\langle 111 \rangle$

Figure 12: Pole figures associated with the 413 grains FDO (RD: rolling direction; TD: transverse direction).

4.4 Calibration of germination energy based on DSC

The remaining parameters to be identified are the severity of transformation β_s and the instant germination barrier $d\mathfrak{g}(j, i, dt = 0)$. DSC scan results, shown in Figure 3 have to be reused for that purpose. The Gibbs free energy density mapping is first built. It has been shown in [12] that β_s, seen as temperature independent in the framework of reversible modeling, is related to the maximal heat flux $q_m(\text{W.m}^{-3})$ of a DSC peak emission (using A to R phase or R to M emission peak), variation of enthalpy and entropy densities (Δh and Δs) and temperature rate $\dot{T}$ used during the experiment (Equation 77).

$$\beta_s = -\frac{4q_m}{\dot{T}\Delta s \Delta h} \tag{77}$$

Based on the pre-defined Gibbs free energy density mapping and initial β_s, a first Boltzmann reversible based DSC simulation is processed (result is shown in Figure 13a). β_s is then used to define the appropriate unit volume V_u at the transformation temperature. A second simulation using a temperature dependent β_s can be performed (Figure 13b). We assume next that all transformation types $\mu \to (j \to i)$ share the same germination barrier $d\mathfrak{g}^c$ related to the delay

between forward and reverse DSC peaks. The germination barrier $d\mathfrak{g}(j,i,dt=0)$ for all transformation types verifies:

$$d\mathfrak{g}^c(i,j,t=0) = d\mathfrak{g}^c(dt=0)\,\forall(i,j), i \neq j \tag{78}$$

$$d\mathfrak{g}^c(i,i,dt=0) = \infty\,\forall i \tag{79}$$

The strong penalty used in the second relation is introduced to forbid any self transformation. After several tries, the uniform germination barrier $d\mathfrak{g}^c$ can be estimated (Figure 13c). Optimized values for NiTi used in the experiments are:

$$N = 1e5; \tag{80}$$

$$c = 8.5 \times 10^{-7}\,\mathrm{s}^{-1} \tag{81}$$

$$d\mathfrak{g}^c(dt=0) = \frac{-\log(c)}{\beta_s} = 15.2 \times 10^6\,\mathrm{J\,m}^{-3} \tag{82}$$

A third (and more correct) simulation of DSC is obtained. But as we can see in Figure 13c, the transformation delay does not differ for M to R forward and R to M reverse peaks. Indeed the lowest crystalline symmetry of martensite variants induces the largest meta-stability barrier for other variant types to transform into. The additional non-compressible germination term $d\mathfrak{g}^a$ is consequently considered for the transformation of austenite and R phase into martensite ($d\mathfrak{g}^a_{A-M}$ and $d\mathfrak{g}^a_{R-M}$) in order to reduce the temperature hysteresis for A-R transformation keeping a high M-R hysteresis. Optimized values are given below:

$$d\mathfrak{g}^a_{A-M} = 6.5 \times 10^6\,\mathrm{J\,m}^{-3}\ \forall(i,j), i \neq j \tag{83}$$

$$d\mathfrak{g}^a_{R-M} = 5.5 \times 10^6\,\mathrm{J\,m}^{-3}\ \forall(i,j), i \neq j \tag{84}$$

$$d\mathfrak{g}^a_{A-R} = 1 \times 10^6\,\mathrm{J\,m}^{-3}\ \forall(i,j), i \neq j \tag{85}$$

- $(j,i) \rightarrow$ Transformation between A/M $\qquad d\mathfrak{g}^a(j,i) = d\mathfrak{g}^a_{A-M}$
- $(j,i) \rightarrow$ Transformation between R/M $\qquad d\mathfrak{g}^a(j,i) = d\mathfrak{g}^a_{R-M}$
- $(j,i) \rightarrow$ Otherwise $\qquad d\mathfrak{g}^a(j,i) = d\mathfrak{g}^a_{A-R}$

The global germination barrier is finally given by:

$$d\mathfrak{g}(j,i,dt) = d\mathfrak{g}^c(dt) + d\mathfrak{g}^a(j,i) \tag{86}$$

With this ad-hoc correction, the numerical simulation of DSC process converges towards the experimental observation as illustrated in Figure 13d.
However it can be observed that the simulated transformation peak from R phase towards martensite is 'sharper' than the experimental one. Indeed, β_s parameter (and associated unit volume) is identified using only one peak (here the A to R-phase peak) of two possible peaks, supposing a same *shape* of the two peaks. This is not the case. Improvements are possible and will be addressed in conclusion, but this drawback is not detrimental for other modeling aspects.

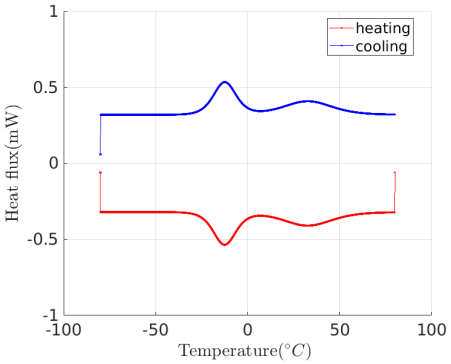

(a) Simulation with reversible Boltzmann model and β_s defined as a constant

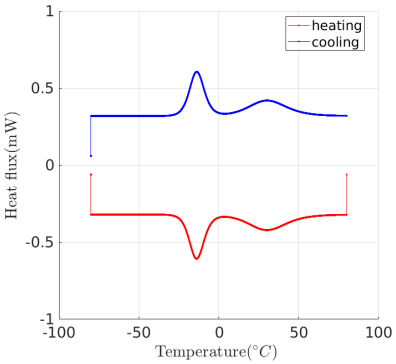

(b) Simulation with reversible Boltzmann model and $\beta_s = \frac{V_{unit}}{k_b T}$

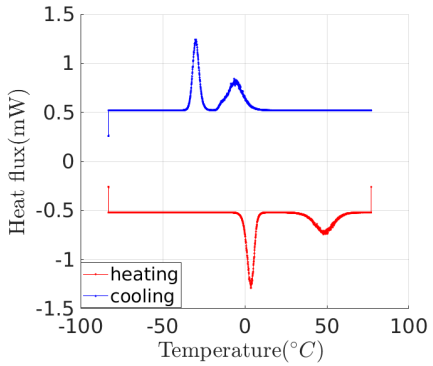

(c) Simulation with uniform germination barrier - 1500 tests

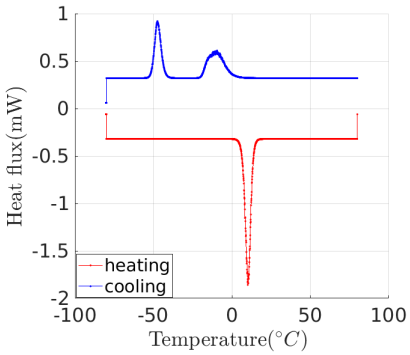

(d) Simulation with $dg_{A\to M} = 6.5 \times 10^6\,\mathrm{J\,m^{-3}}$ - 1500 tests

Figure 13: Germination barrier calibration based on DSC scan, $\dot{T} = 5\,\mathrm{K\,min^{-1}}$

5 Several examples of virtual tests

In this section, a series of virtual loading of Ni-Ti polycrystal (using the parameters identified in the previous section) is proposed. This series allows an illustration of the performance of the energy based stochastic model to be presented. Among those, we choose to present simulations, from the most classical to the most challenging cases: pseudo-elasticity under tension and compression at various temperature and stress rate, one-way shape memory effect under tension and compression, two ways shape memory effect and 2D plane-stress loading (deformation threshold, non proportional loading).
It must be underlined as a major point that a validation of the modeling by a point to point comparison to experimental results would require to implement the RVE model in a numerical model (see for example the finite difference approach developed in [11]). Indeed, the stochastic multiscale model is unable to reproduce strain localization bands as observed in the experiments reported in subsection 4.3 and in many other experiments reported in the literature. A strict validation is consequently not reachable since we only present in this paper a modeling of RVE. For the same reason (thermal boundary conditions cannot be modeled), the heat emission (or absorption) due to phase transformation was neglected in most simulations presented in this section ($k = \infty$). Anisothermal situations are illustrated only for the 1D tensile loading at the end of this section. In the following, some Gibbs free energy density of variants are plotted vs. time for a single crystal tensile strained along the $< 111 >$ axis of the austenite parent phase $(\Phi_1 = -\pi/2, \Psi = -acos(1/\sqrt{3}), \Phi_2 = \pi/4)$. Plots giving the average phase volume fractions concern the entire RVE.

5.1 Simulation of 1D tensile loading

A quasi-static stress-controlled tensile loading and unloading is simulated at two different temperatures $T = 293K$ and $T = 303K$, the loading protocol is synthesized as follows:

- 1D Load at $T = 303K$: Apply stress-controlled load and unload with a speed $v = 1\,\mathrm{MPa\,s^{-1}}$ at $T = 303K$, with a maximum amplitude of $\sigma_{max} = 500\,\mathrm{MPa}$
- 1D Load at $T = 293K$: Apply stress-controlled load and unload with a speed $v = 1\,\mathrm{MPa\,s^{-1}}$ at $T = 293K$, with a minimum amplitude of $\sigma_{max} = 500\,\mathrm{MPa}$

Figure 14 shows respectively: the associated temporal evolution of phases volume fractions, the Gibbs free energy density evolution of each variant in the selected grain, and the modeled stress-strain response of the material at different temperatures. The general comments that can be given are:

- General trends for Ni-Ti pseudo-elastic behavior are observed, in accordance with experiments reported in the literature [33]; the mechanical hysteresis is remarkably modeled;
- The RVE has been fully transformed at maximum stress load leading to an axial transformation strain of about 11%. This deformation level may appear too high. This is a common defect when a homogeneous stress assumption is used [13]. Value reached is however in accordance with the parameters of the Bain matrices.
- At $T = 303$K, martensite transformation is fully accomplished at a higher maximum stress level compared to $T = 293K$.
- The phase transformation threshold increases following a temperature sensitivity of about $\Delta\sigma/\Delta T \simeq 6.4\,\mathrm{MPa\,K^{-1}}$.

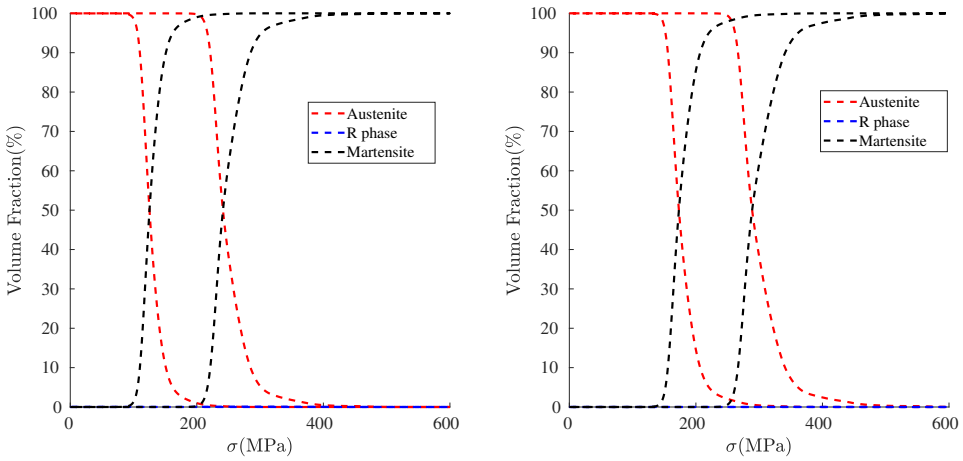

(a) Phases volume fraction as function of stress: (Left)$T = 293\,\mathrm{K}$ (Right) $T = 303\,\mathrm{K}$

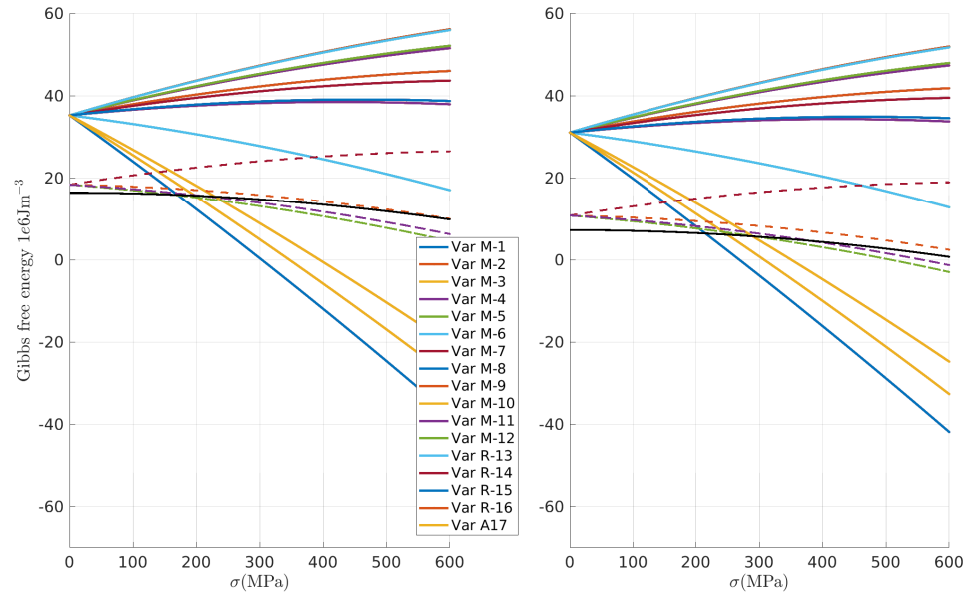

(b) Gibbs free energy density evolution of each variant:(Left)$T = 293\,\mathrm{K}$ (Right) $T = 303\,\mathrm{K}$

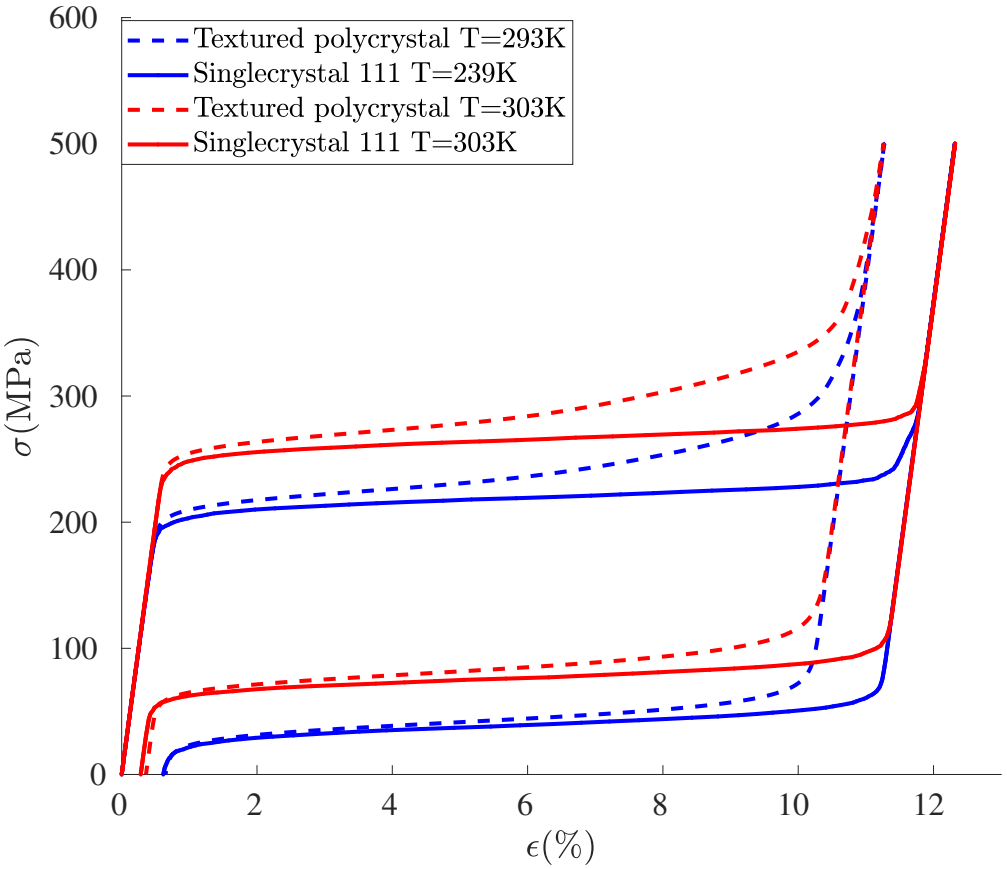

(c) Numerical stress/strain response at the two different temperatures for single and polycrystal

Figure 14: 1D tensile loading/unloading at different room temperatures.

5.2 Simulation of 1D tension-compression loading

In literature, for nearly equiatomic NiTi SMA at room temperature, the stress threshold in compression is slightly higher than in tension ([26]). A virtual loading is applied in order to simulate this asymmetry. The loading protocol can be summarized in:

- 1D stress-controlled tensile load and unload with a speed $v = 1\,\mathrm{MPa\,s^{-1}}$ at $T = 293K$, with a maximum amplitude of $\sigma_{max} = 500\,\mathrm{MPa}$
- 1D stress-controlled compression load and unload with a speed $v = 1\,\mathrm{MPa\,s^{-1}}$ at $T = 293K$, with a maximum amplitude of $\sigma_{min} = -500\,\mathrm{MPa}$

Figure 15 shows respectively: the Gibbs free energy density evolution of each variant in the selected grain, numerical stress/strain response for polycrystal and single crystal strained along $< 111 >$ direction and the associated temporal evolution of phases volume fractions. The general comments that can be given are:

- General expected trends are observed (see some typical experimental results by [14]);
- In Figure 15a, it is clearly observed that martensite variants activated during tension are different from martensite variants activated during compression;
- This selection leads to the asymmetry observed for the tension vs. compression stress-strain response (Figure 15b), and is consistent with experimental observations [14];
- Under compression, the presence of R-phase is observed during both the loading and unloading stages before austenite transformation starts. As seen in Figure 15a for single crystal loaded along $< 111 >$ direction, the R phase variant (R14) has the lowest Gibbs potential at $\sigma_{min} = -500\,\mathrm{MPa}$. Consequently a large volume fraction of R phase is expected after full loading and unloading, as seen in Figure 15c, which induces a significant residual strain of about $\epsilon_{res} = 2\%$. On the contrary, under tension, several martensite

variants are more stable than the R phase variants at higher stress level. As a result, the volume fraction of R phase as predicted by the simulation is low. The presence/non-presence of R phase is potentially the principal factor inducing the asymmetrical behavior between tension and compression. It leads on the other hand to an initial threshold in compression apparently close to the threshold in tension for the single crystal loaded along ⟨111⟩ direction. However a numerical test carried out at higher compression stress shows that a R → M transformation occurs at −1000 MPa, allowing the expected tension/compression asymmetry to be obtained.

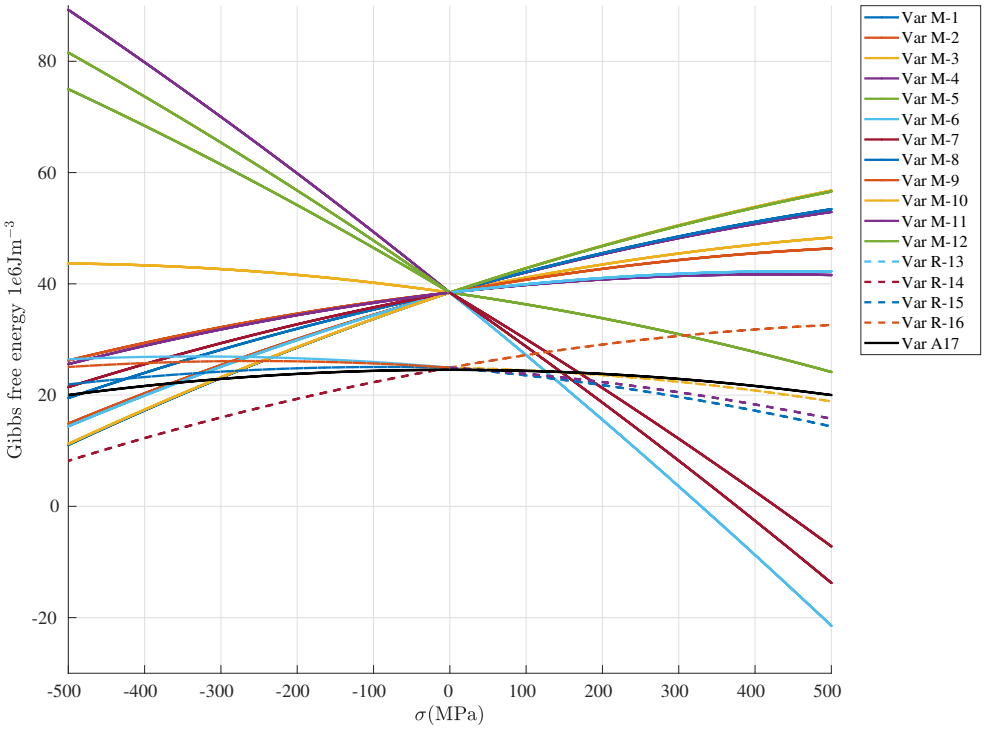

(a) Gibbs free energy density evolution of each variant for a single crystal strained along < 111 > direction.

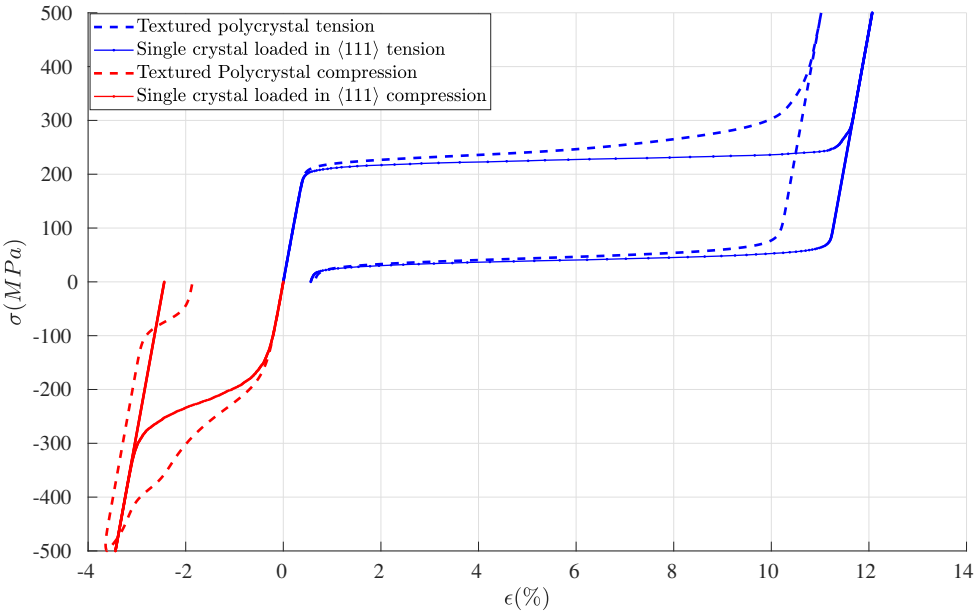

(b) Axial stress/strain response

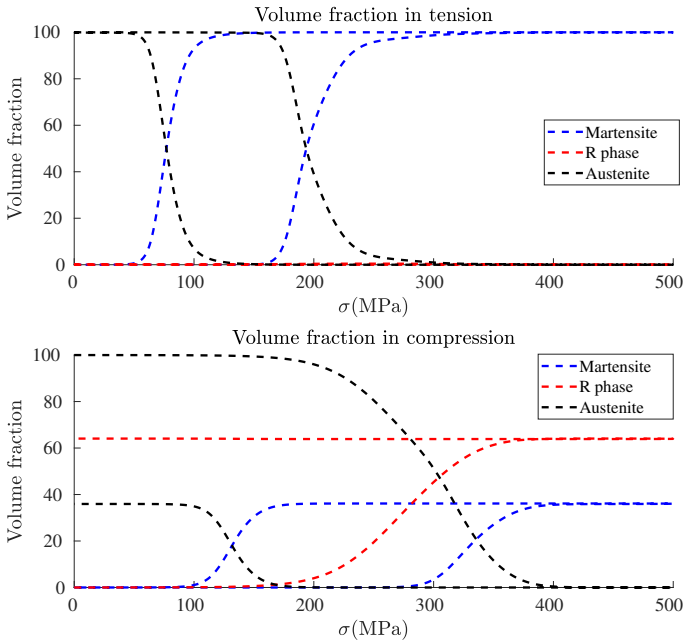

(c) Phases volume fraction as function of stress for tension(up) and compression(down) for a single crystal strained along $< 111 >$ direction.

Figure 15: 1D tension/compression loading at room temperature (T=293 K

5.3 Pseudoelasticity and partial load

In this subsection, some partial tensile loading/unloading tests have been simulated, corresponding to a situation where the stress level is insufficient to fully transform the austenite into martensite. This simulation especially allows the effect of temporal relaxation associated with the germination barrier to be illustrated. The following loadings are considered:

- Full Tensile Load: stress-controlled tensile load and unload with a speed $v = 1\,\mathrm{MPa\,s^{-1}}$ at $T = 293K$, with a maximum amplitude of $\sigma_{max} = 500\,\mathrm{MPa}$
- Partial Tensile Load 1: stress-controlled tensile load and unload with a speed $v = 1\,\mathrm{MPa\,s^{-1}}$ at $T = 293K$, with a maximum amplitude of $\sigma_{max} = 190\,\mathrm{MPa}$
- Partial Tensile Load 2: stress-controlled tensile load and unload with a speed $v = 1\,\mathrm{MPa\,s^{-1}}$ at $T = 293K$, with a maximum amplitude of $\sigma_{max} = 190\,\mathrm{MPa}$; stress is kept constant for 200s at the maximum stress amplitude level before unloading.

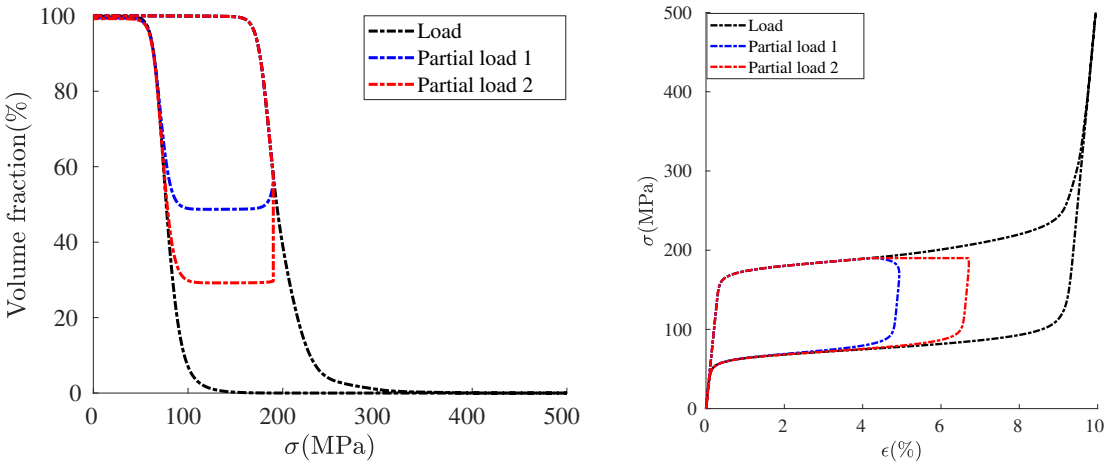

(a) Austenite volume fraction as function of stress

(b) Stress/strain simulation

Figure 16: 1D tension/compression partial loadings at room temperature (T=293K)

The comments that can be given are:

- As we can see in Figure 16a and Figure 16b, the partial load 1 illustrates the germination barrier delays in two transformation directions ($A \rightarrow M$ and $M \rightarrow A$). For partial load 1, when stress unload begins, the RVE is still far away from equilibrium state, thus the stress/strain curve does not immediately go back to the elastic regime. A narrow non linear region is needed to overcome the germination barrier for $M \rightarrow A$ transformation initiation.
- However, if we hold the stress level as constant for a long time instead of immediately unload the sample (case of partial load 2), transformation from $A \rightarrow M$ and deformation still increases until a certain martensite volume fraction is reached. This is a direct example of temporal relaxation for germination barrier. When the Gibbs free energy density between variants is not enough to bypass instant germination barrier, it takes a longer time to converge towards the equilibrium state (see Equation 37).
- For the case of partial load 2, the unload begins after the NiTi SMA reaches its equilibrium state (see Figure 16a). At that time, the polycrystal needs to bypass a germination barrier before any $M \rightarrow A$ transformation initializes, leading to an elastic unloading part.
- This point illustrates that an extremely low strain rate would be required to reach the 'true' static behavior, due to the time constant associated with the stochastic process. Stress threshold and hysteresis loop are sensitive to this process, superimposed to classical thermal effects (not accounted for in this simulation).

5.4 Simulation of one way shape memory effect(OWSME)

The one way shape memory effect of SMA appears when the alloy is in its cold state (below austenite start temperature $T \leq A_s$, mainly indicating a martensite state). The alloy can be stretched and still hold the permanent deformation after unloading, until it is heated above the $M \rightarrow A$ transition temperature [29] when the deformation is recovered. We propose hereafter to simulate a one way shape memory effect for both tension and compression of NiTi polycrystal. Let consider the following steps illustrated by letters (A to K):

- From A to F:
  - A $\rightarrow$ B: NiTi polycrystal is cooled at $T = 263\,\mathrm{K}$;
  - B $\rightarrow$ C $\rightarrow$ D: a tensile loading up with a maximum stress $\sigma_{max} = 100\,\mathrm{MPa}$ is first applied. The material is then unloaded to zero;
  - D $\rightarrow$ E $\rightarrow$ F: the material is heated up to $T = 373\,\mathrm{K}$ (above the $M \rightarrow A$ transformation temperature) and then cooled to $T = 263\,\mathrm{K}$.
- From F to J: the same steps are applied under compression

Figure 18a and 18b plot the associated variation of Gibbs free energy density and variants volume fraction respectively in the reference single crystal.
The comments that can be given are:

- Initial cooling shifts points in Figure 17 from A to B (or E to F for compression). At point B and F. It must be first observed that R phase is dominant at this temperature. R phase variants are equiprobable (equivalent in volume fraction) as illustrated in Figure 18b. By applying the stress loading, R phase variants whose transformation strain is mainly oriented along the loading direction are favored in tension. The same variants are unfavored under compression leading to an asymmetric selection of variant types and numbers (in accordance with their Gibbs free energy density as illustrated in Figure 18a). Selected variants remain stable during unloading between C and D (or G and H under compression), leading to a permanent strain even when the stress is completely removed. The associated maximum eigenvalue of transformation matrix for R phase is around $\epsilon_{max} \simeq 2\%$, which explains the maximum value for permanent strain observed during OWSME cycle. Despite some few differences of stress threshold, results of the modelling are in very good agreement with the experimental results reported in [20].
- Asymmetry of OWSME between tension and compression is clearly illustrated in relation with the asymmetric selection of variant types and numbers in grains, although the reorientation mechanism between tension and compression has nearly the same stress threshold according to the definition of the germination energy. Indeed, it is possible following the proposition of some authors [30] to make a more complete identification of germination matrix $\mathbf{dg}(\mathbf{i}, \mathbf{j})$ that could lead to an improvement of the modeling results.

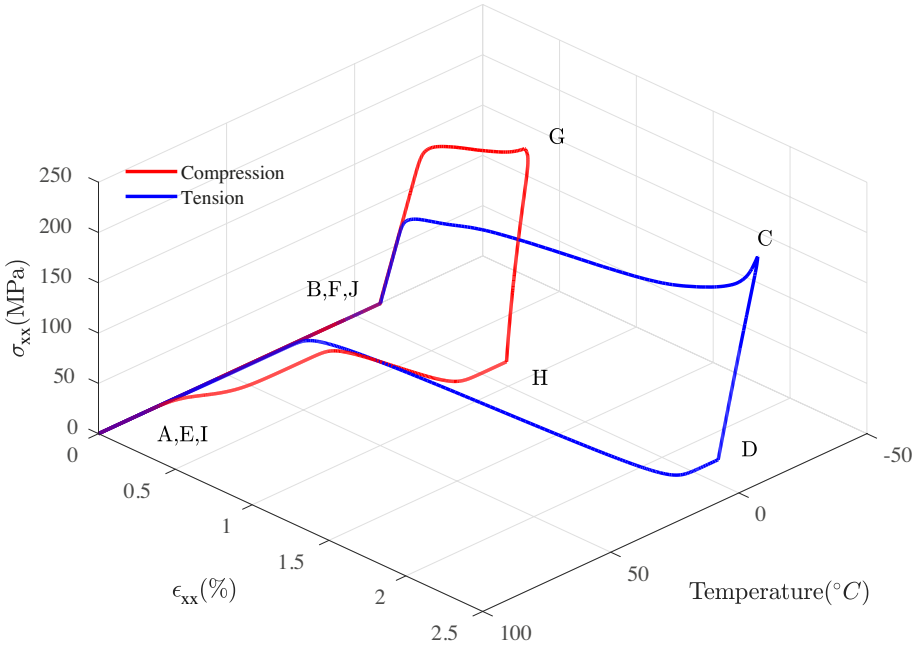

Figure 17: Simulation of OWSME in tension and compression

5.5 Simulation of stress-assisted two ways shape memory effect (SA-TWSME)

Stress-assisted two ways shape memory effect refers to the fact that SMA may remember two different shapes: one at high temperature and the other at low temperature. A material that exhibits a shape memory effect during both heating and cooling is a two ways shape memory effect material. The loading path that helps to produce the two ways shape memory effect of NiTi polycrystal (reference points are illustrated in Figure 19a) is the following:

- A-B-C-D: 1D tensile loading is applied to NiTi SMA. The stress is held as constant $\sigma = 250\,\text{MPa}$, and a thermal cycle consisting of a constant rate heating and cooling is applied with a maximum amplitude $T_{max} = 373\,\text{K}$.
- D-E-F-G: From the end point of previous cycle, the applied stress is raised up and held as constant $\sigma = 300\,\text{MPa}$, and a second thermal cycle consisting of a constant rate heating and cooling is applied with a maximum amplitude $T_{max} = 373\,\text{K}$.

Figure 19a illustrates the associated stress-strain behavior. The simulation plotted in Figure 19b illustrates how the thermal loading at two different stress levels ($\sigma = 250, 300$ MPa) can change the volume fraction of the different phases. For the two cycles investigated, the NiTi polycrystal always returns to its shape at the end of thermal loading. At higher stress level start ($\sigma = 300$ MPa), the thermal hysteresis area is higher because of a higher amount of martensite phase involved in the transformation (Figure 19b). The higher temperature threshold at high stress level for SA-TWSME can be explained by the fact that martensite variants are more stable. A higher temperature is required to destabilize this phase. Again, to the best knowledge of authors, very few models are able to simulate such kind of complex behavior, for single or polycrystals.

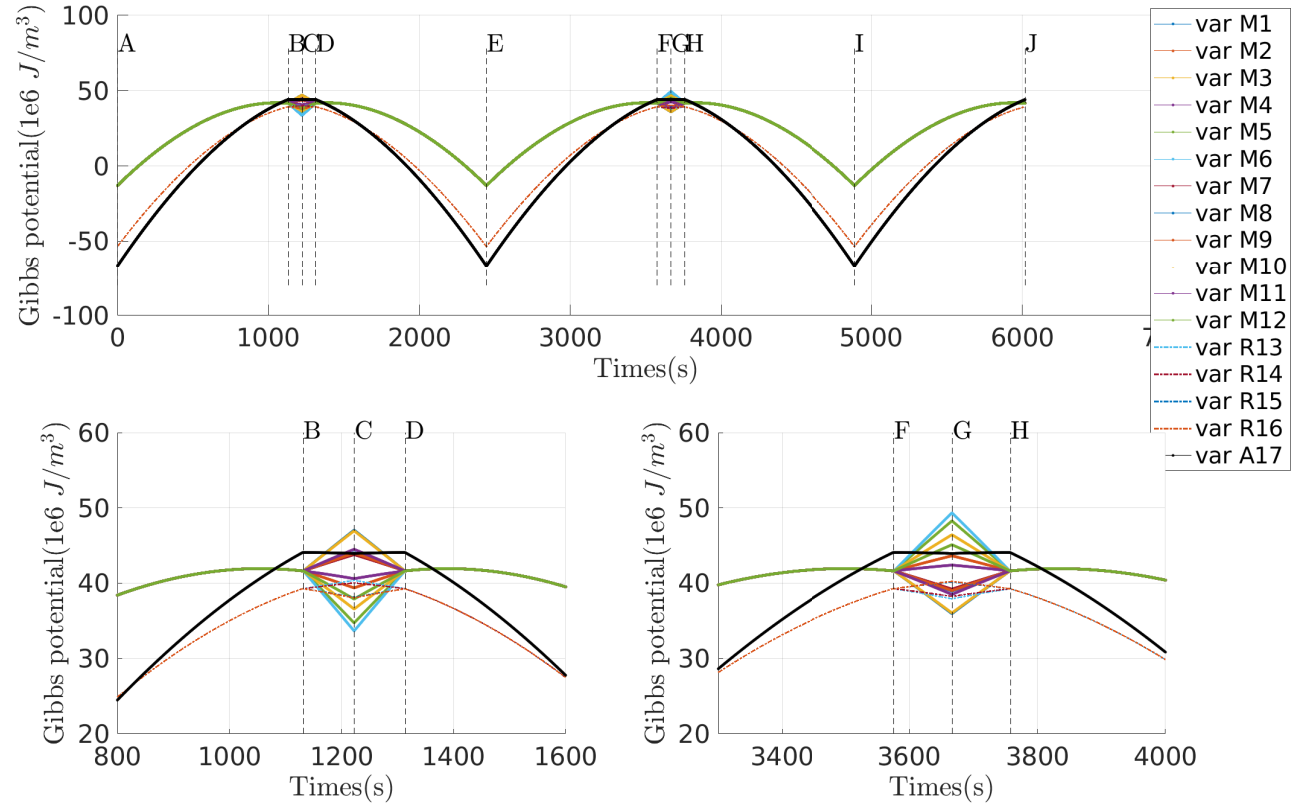

(a) Gibbs free energy density of variants

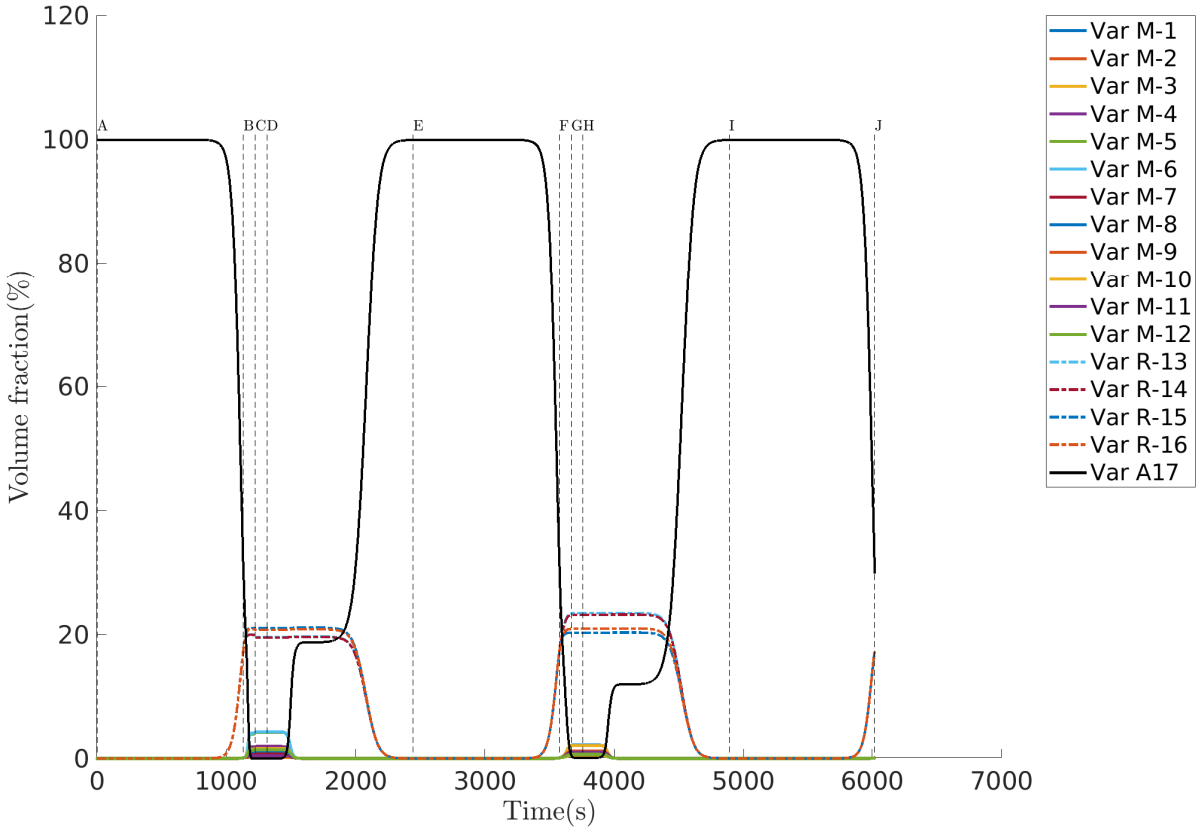

(b) Variants volume fraction evolution

Figure 18: The evolution of Gibbs free energy density of variants

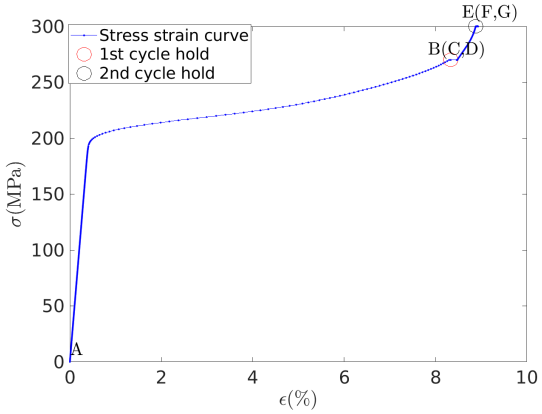

(a) Applied 1D tensile load and two thermal cycles

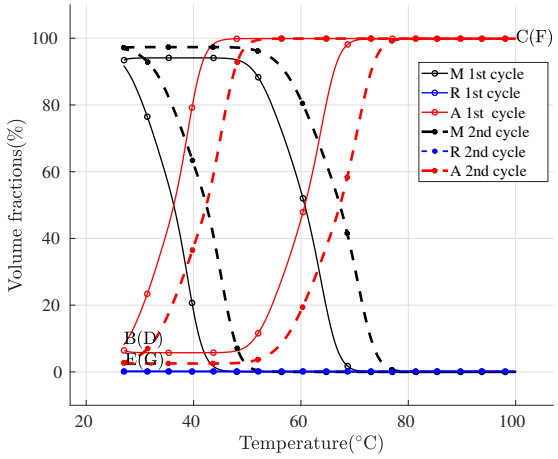

(b) Average volume fractions of A, M and R phases as function of temperature

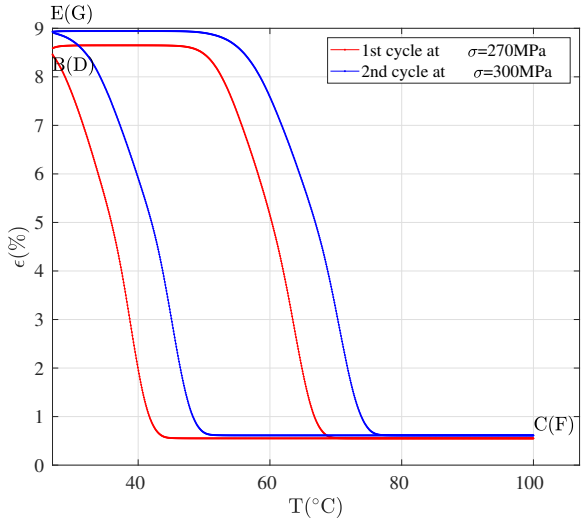

(c) Numerical strain-temperature response for NiTi polycrystal

Figure 19: Stress-assisted two ways shape memory effect

5.6 Proportional / non proportional biaxial loading - 2D phase mapping

The stochastic multiscale model can simulate the effect of a multiaxial mechanical loading. Its intrinsic hysteresis makes of course the loading path part of the model's response. Situations that can be tested are then innumerable. We decided to focus on a simple biaxial loading since some biaxial experiments are available in literature allowing a model/experiment comparison. A proportional stress-controlled loading is first applied on the polycrystal given by :

$$\boldsymbol{\sigma} = s(t) \begin{pmatrix} \cos\theta & 0 & 0 \\ 0 & \sin\theta & 0 \\ 0 & 0 & 0 \end{pmatrix} \tag{87}$$

$$s(t) = [0:1:1000\ 1000:-1:0] \text{ MPa} \tag{88}$$

$$\theta = [0:5:355] \text{ degree} \tag{89}$$

The forward transformation is defined for proportional load $s(t) = [0:1:1000]$ MPa and the backward transformation is defined for corresponding unload $s(t) = [1000:-1:0]$ MPa. Each simulation is performed at constant angle θ for a constant temperature T=303K. The simulation is repeated for each angle, allowing a discrete mapping of the stress plane. Many figures can of course be drawn. We decided to illustrate this loading by plotting the volume fraction of A, R

and M phases during loading and unloading (see respectively Figure 20a to Figure 21d). These figures illustrate clearly the global shape of the transformation threshold in the stress plane.

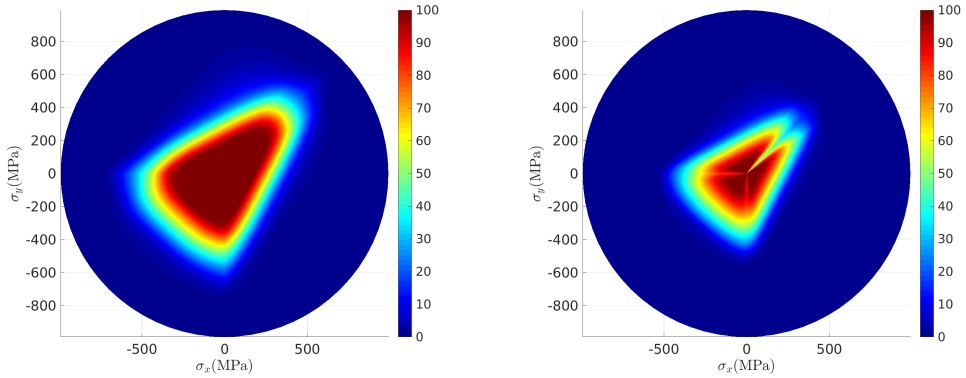

(a) Loading (b) Unloading

Figure 20: Austenite phase mapping under proportional stress condition.

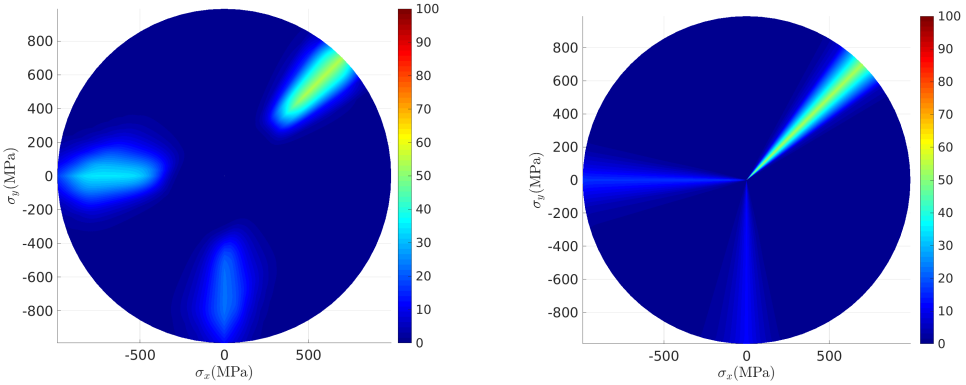

(a) R-phase - Loading (b) R-phase - Unloading

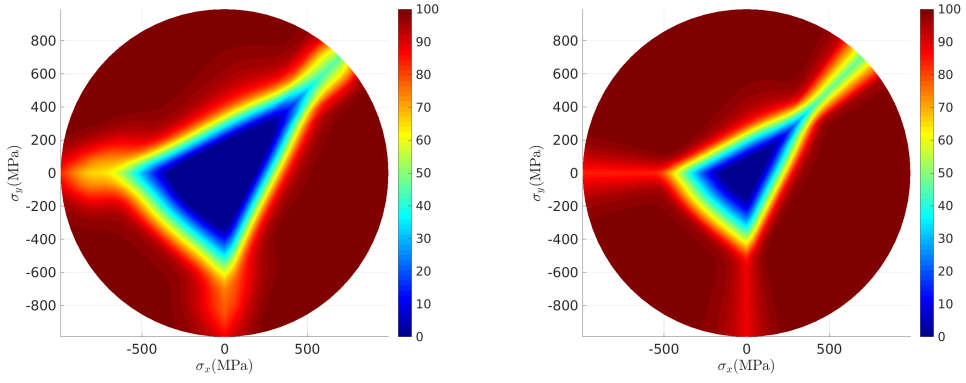

(c) Martensite - Loading (d) Martensite - Unloading

Figure 21: R phase and martensite phase mapping under proportional stress condition.

As expected, the forward transformation leads to a larger stress threshold compared to backward transformation, and the hysteresis between loading and unloading is consistent. However, there exists an unexpected area (narrow cone) where R phase concentration remains high along $\sigma_1 = \sigma_2$ axis ($\sigma > 0$). Indeed, depending on their orientation, a significant amount of grains does not transform from R to M phase under equibiaxial loading. The Gibbs free energy density of some R phase variants remains lower than the Gibbs free energy density of some corresponding M phase variants whatever the stress level ! Some validation of such result would require for example in-situ XRD measurement as proposed in [6].

Transformation thresholds under biaxial loading are available in literature [22][20]. They are always defined using a deformation criterium. Figure 22 illustrates the transformation threshold from the SMSM for an equivalent transformation strain of 0.6% at 293 K and 303 K (a Levy-Mises equivalent strain (Equation 90) has been chosen to define the deformation criterium). This result is in very good agreement with experimental results and the phenomenological modeling of [22].

$$\epsilon_{eq}^{tr} = \sqrt{\frac{2}{3}\boldsymbol{\epsilon}^{tr} : \boldsymbol{\epsilon}^{tr}} \tag{90}$$

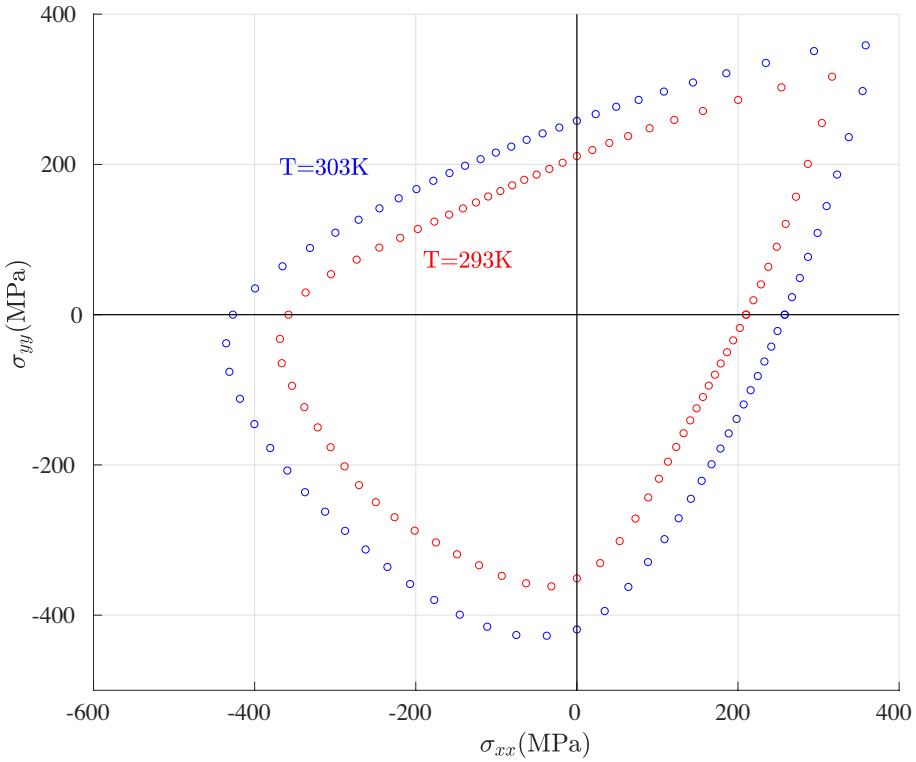

Figure 22: Simulation of the transformation threshold defined by Levy-Mises equivalent transformation strain at 0.6% for NiTi polycrystal at 293 K and 303 K.

The stochastic multiscale model is an hysteretic modeling. Non proportional loading and sensitivity to stress path can consequently be tested. These points are highlighted in the next figures where the following paths have been used in $(\sigma_{xx}, \sigma_{yy})$ plane:

- Path 1: a quasi static stress-controlled uniaxial loading is first applied along $\vec{x}$ until $\sigma_{xx} = 600$MPa is reached. This stress is hold and a second stress loading is gradually applied along $\vec{y}$ direction until σ_{yy}=600 MPa, reaching the equibiaxial point $(\sigma_{xx}, \sigma_{yy}) = (600, 600)$ MPa.
- Path 2: $\vec{x}$ and $\vec{y}$ axes have been inverted comparing to path 1. The final stress point is exactly the same.

As we can see in Figure 23, the strain (total strain) response of NiTi polycrystal for paths 1 and 2 is nearly symmetrical regarding to $\epsilon_{xx} = \epsilon_{yy}$ axis (ϵ_{zz} component exists but has not been plotted), in accordance with the transverse isotropic texture of the material, but the strain levels at the final point are strongly different highlighting the strong non-linear and hysteretic character of the material behavior. Some comparisons with experiments should be necessary too to validate the modeling.

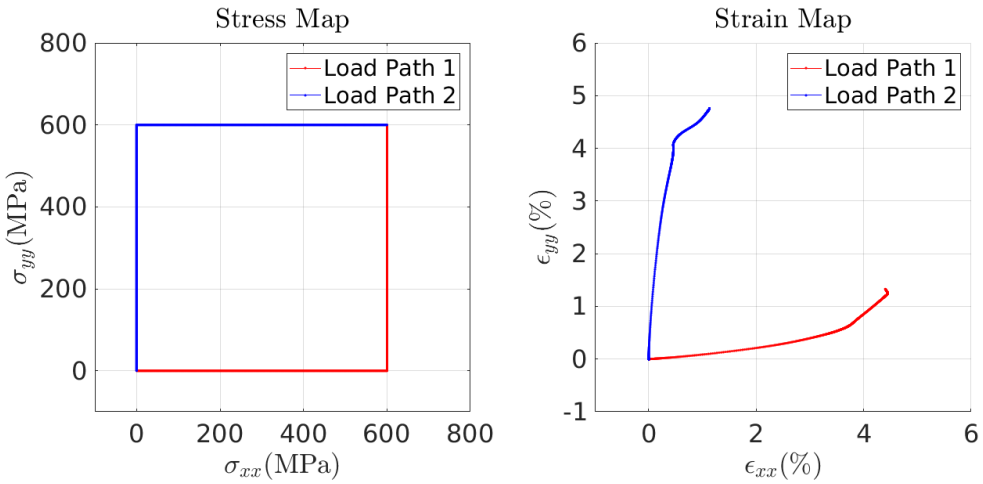

Figure 23: Illustration of the material behavior in case of non proportional loading and sensitivity to the stress path: Stress and corresponding total strain paths

5.7 Pseudoelasticity and heat dissipation

All numerical simulations presented in this section until now have been obtained using isothermal condition ($k = \infty$). This choice has been made for an easier interpretation of results and because an anisothermal condition can be seen as artificial for the modeling of a RVE. The influence of heat dissipation and exchange of NiTi polycrystal can however be illustrated for all previous cases. It must be kept in mind that the validity of the results remains questionable considering the fact that a RVE is not a structure. A simple test case is proposed as an illustration: it is a 1D tensile stress controlled loading and unloading, using a stress rate $\dot{\sigma} = 1\,\mathrm{MPas}^{-1}$ and a maximum stress $\sigma_{max} = 600\,\mathrm{MPa}$ at $T = 293K$ (initial and ambient temperature). Three different heat dissipation conditions are applied:

- Adiabatic: $k = 0$ J.m^{-3}.K^{-1}
- Isothermal: $k = \infty$ (see subsection 5.1)
- moderate heat exchange: $k = 11.5\,\mathrm{kW\,m^{-3}\,K^{-1}}$. This value corresponds as a heat exchange coefficient of about $20\,\mathrm{W\,m^{-2}\,K^{-1}}$ for the sample presented in Figure 6.

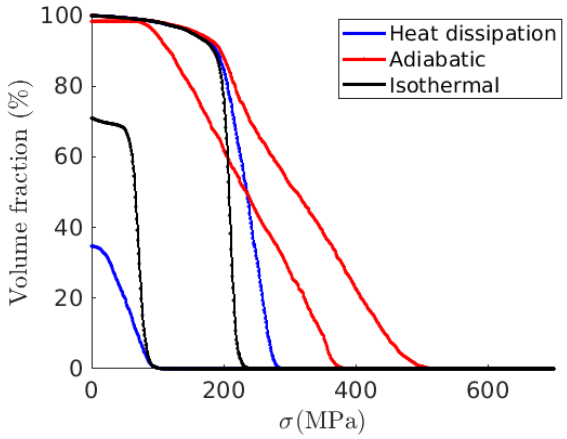

(a) Evolution of variants volume fractions as function of stress for the selected grain

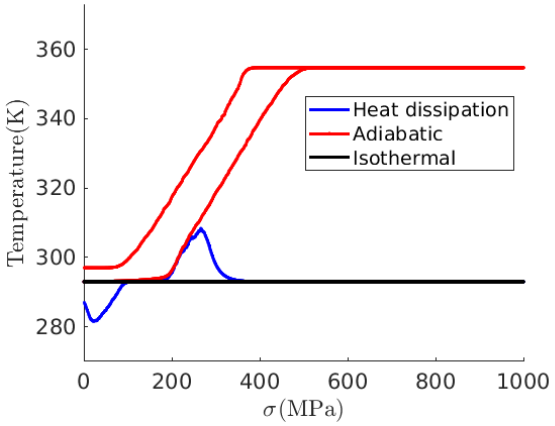

(b) Temperature evolution as function of stress

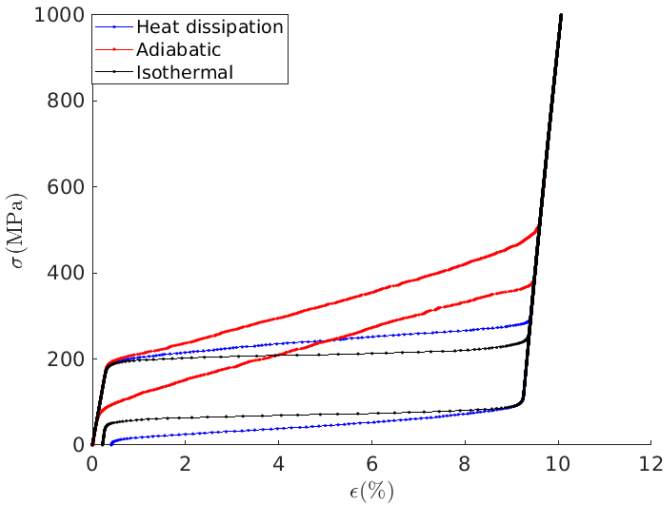

(c) stress-strain curves

Figure 24: Illustration of pseudoelastic behavior from SMSM depending on thermal conditions and comparison to experimental data for NiTi SMA.

The following comments can be proposed:

- Anisothermal situation has already been discussed. It corresponds to a perfect convection (or conduction) situation describing a quasistatic transformation;
- As we can see in Figure 24b, the emission of latent heat due to $A \rightarrow M$ phase transformation leads to a very high temperature increase reaching up to T=355 K for the adiabatic situation. This temperature increase is accompanied by a concomitant phase transformation threshold increase (see Figure 24c). Of course, the initial temperature of NiTi polycrystal ($T = 293K$) is almost fully recovered during unloading due to the heat absorption associated with the backward phase transformation ($M \rightarrow A$);
- In case of moderate heat exchange, the latent heat due to $A \rightarrow M$ phase transformation acts as heat source that brings to a temperature increase up to $T = 305K$ during loading. Indeed a part of power source is transmitted to the (virtual) surrounding medium. The temperature of NiTi polycrystal decreases next to $T = 282K$ during the unloading reaching a temperature below the ambient temperature. These small temperature variations result in a moderate stress threshold increase during loading and a moderate stress threshold decrease during unloading. This phenomenon leads to a significant increase of hysteresis area, comparing to the isothermal situation (see Figure 24c). These results are in qualitative agreement with the experimental results from Mac Cormick (1993) [28]. They are in agreement with the macroscopic modeling results and comments from Boyd and Lagoudas (1996) [5] too. The latter highlight in particular the phenomenon of "thermal hardening" of SMA here clearly observed. The same authors also obtained an adiabatic

cycle surface smaller than the isothermal cycle surface, resulting from a temperature assistance effect on transformations. Interpretation of adiabatic cycle surface remains however complex given the co-existence of the three phases.

6 Conclusion

In this paper, a stochastic multiscale thermomechanical modeling of shape memory alloys has been presented. The stochastic description of the volume fraction of phase variants is ensured by a kinetic Monte-Carlo algorithm, using the local Gibbs free energy density as a main input. This model includes an instantaneous description of the germination process from variant to variant. It leads to simulate the hysteretic and non-linear mechanical behavior of SMA and the phase volume fraction kinetic includes the nucleation of the so-called R-phase usually omitted in former models. Only few parameters are required to describe the hysteretic behavior at the grain and RVE scales by successive homogenizations: most of them can be obtained via a simple DSC scan. This model is not, however, a structure model: it only allows the modeling of a RVE. A polycrystalline NiTi has been used to illustrate the parameters identification. However the deformation of this material highlights strong localization bands whose description is unreachable by the modeling. Any comparison between model and experiments for validation purposes is therefore not possible. A crucial stage must consist in the implementation of this model in a structure calculation using finite elements or finite differences modeling.
The various illustrations proposed (therefore assuming the material to be homogeneous) are nevertheless in very good qualitative agreement with the various experimental results reported in the literature. : DSC scan; pseudo-elasticity under tension and compression; hysteresis loops for partial transformation; one way shape memory effect and stress-assisted two ways shape memory effect; tension-compression asymmetry, biaxial proportionnal and non-proportional loading effects.
To the best knowledge of authors, no phenomenological model has demonstrated such capabilities to describe so completely a so wide diversity of behaviors. The model demonstrated its strength especially when phase transformation induced by multi-axial thermomechanical load was not fully finished and unloading begins. [18] and [30] has presented a summary of most classical existing models in the recent twenty years. A brief comparison between several most classical models including our model is proposed in Table 6, underlining the relatively universal character of the present modeling. On the other hand, the robustness and simplicity of stochastic modeling must be underlined: for example, the computation time to obtain a 2D transformation stress threshold (3.6×10^6 stress points !) takes 8 hours for the investigated NiTi polycrystalline containing 413 grains (about 8 ms per point) with a processing power of 20 parallel $\times 2.2$ GHz computers. Improvements are however possible. It has been for example shown that the R-phase to martensite peak emission during a DSC scan is not properly modeled (insufficient width). Indeed the mechanical incompatibility is not taken into account at the variant scale. The implementation of a spatial heterogeneity of germination and associated variants prohibition (see the work of [36]) would probably slow down the transformation. The definition of a specific interaction matrix is another possible solution to take these phenomena into account in a modeling, as proposed by [35] and [31]).
No validation of the model in the strict sense of the term has been proposed in this paper. As already explained, this essential step can only be done once this model implemented in a structure calculation allowing to adequately reproduce heterogeneous chemical, thermal and mechanical fields. This work is in progress.

Model	Anisothermal	Non-proportional	Internal Variables	Partial load	OWSME	SA-TWSME	Asymmetry	Phase	Velocity	Cyclic loading
[23]	×		z_σ, π_f				×	A/M		
[30]	×		H^{mn}			×		A/R/M		
[7]	×		$K(T), Q(t), Y_{vp}(t)$			×		A/M	×	×
[18]	×	×	ξ^f, ξ^r, p^{re}				×	A/M	×	
[15]	×		$\mu_M, \mu_R, \sigma^*_M, \sigma^*_R$					A/R/M	×	×
KMC	×	×	$f(i,t)$	×	×	×	×	A/R/M	×	×

Table 6: Comparison of some thermodynamic models for SMA.

Appendices

A Kinetic Monte-Carlo algorithm flowchart at grain scale

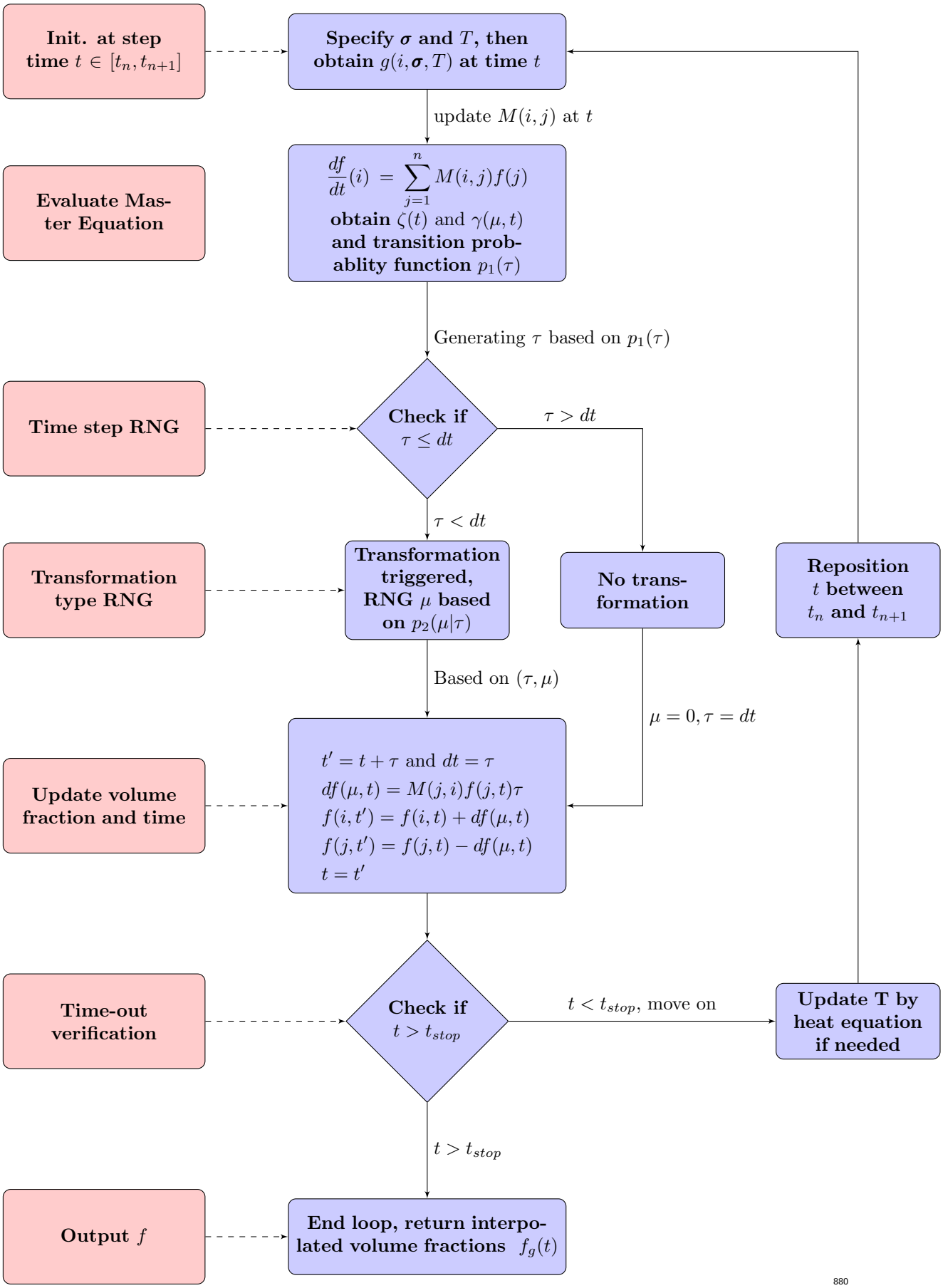

B Inversion Monte-Carlo Method to implement Monte-Carlo step

The description of KMC in subsection 3.4 is nearly complete, except for how we randomly generate transformation variables (τ, μ) at each step (this pair of variable is usually called 'Monte-Carlo step'). In this paper, we adopt the direct method (Inversion Monte-Carlo Method [32] and [3]) to implement the Monte-Carlo step. Another numerical implementation approach (called as 'first transformation method') exists. Both methods have been demonstrated to be exact and rigorous [10]). When the system exceeds three transformation types, the direct method is more sufficient (for the case of Ni-Ti polycrystal, we have 272 different transformation types between variants).

The 'inversion Monte-Carlo method' provides a stochastic application to generate random variables according to prescribed density probability functions, or by using random numbers generated in the unit interval [0,1] (RNG application is available in softwares such as Matlab and C++).

In this appendix, we detail this well known technique for both continuous variable applied for the case of $p_1(\tau) \to \tau$ and discrete variable applied for the case of $p_2(\mu|\tau) \to \mu$.

We seek to generate a random variable y according to the one-variable density function $p(y)$. By definition, the probability that y is generated inside the interval $[y', y' + dy]$ is $p(y')dy$. Based on it, we can build a parent probability function F:

$$F(y) = \int_0^y p(y')dy' \tag{91}$$

Trivially, $F(y_0)$ measures the probability that variable $y \leq y_0$ (this function is defined as probability distribution function). It must be noticed that with the normality of $p(y)$, F is built to have this type of property and its monotony is ensured:

$$F(y = 0) = 0 \text{ and } F(y = \infty) = 1 \tag{92}$$

$$p(y) \geq 0 \tag{93}$$

The basic philosophy of 'inversion method' is that in order to generate a variable y based on $p(y)$, it is easy to select a random number (RN) r belonging to the unit interval $[0, 1]$ and then take for y a value that satisfies:

$$y = F^{-1}(r) \tag{94}$$

Where F^{-1} is the inverse function of F (the existence of F^{-1} is guaranteed by Equation 92 and Equation 93).

Thus considering probability $p_1(\tau)$, the parent function $F_1(\tau)$ can be written as:

$$F_1(\tau) = 1 - \exp(-\zeta\tau) \tag{95}$$

$$\tau = \frac{1}{\zeta} \log(\frac{1}{r}) \tag{96}$$

With r uniformly distributed in the unit interval $[0, 1]$

In discrete case, the procedure is even more trivial. We calculate:

$$F_2(\mu) = \sum_{\mu} p_2(\mu|\tau) \tag{97}$$

$$F_2(\mu - 1) \leq r \leq F_2(\mu) \tag{98}$$

C Convergence of KMC algorithm - influence of independent selections

When a complex thermo-mechanical loading is applied, the crystal system may encounter a scenario where several variants exhibit the same Gibbs free energy density at current time, meaning that the activation of these transformation types are equiprobable.
Unfortunately, KMC randomly choose one of the specific transformation types and moves forward. Convergence to solution is not guaranteed. Other KMC tests are necessary. Indeed, results are probably different but have the same tendency. In stochastic theory, the stochastic average eventually converges towards the macroscopic average when enough independent tests based on probability functions are performed.
Figure 25 illustrates this progressive convergence for DSC simulation with an increasing number of numerical tests.

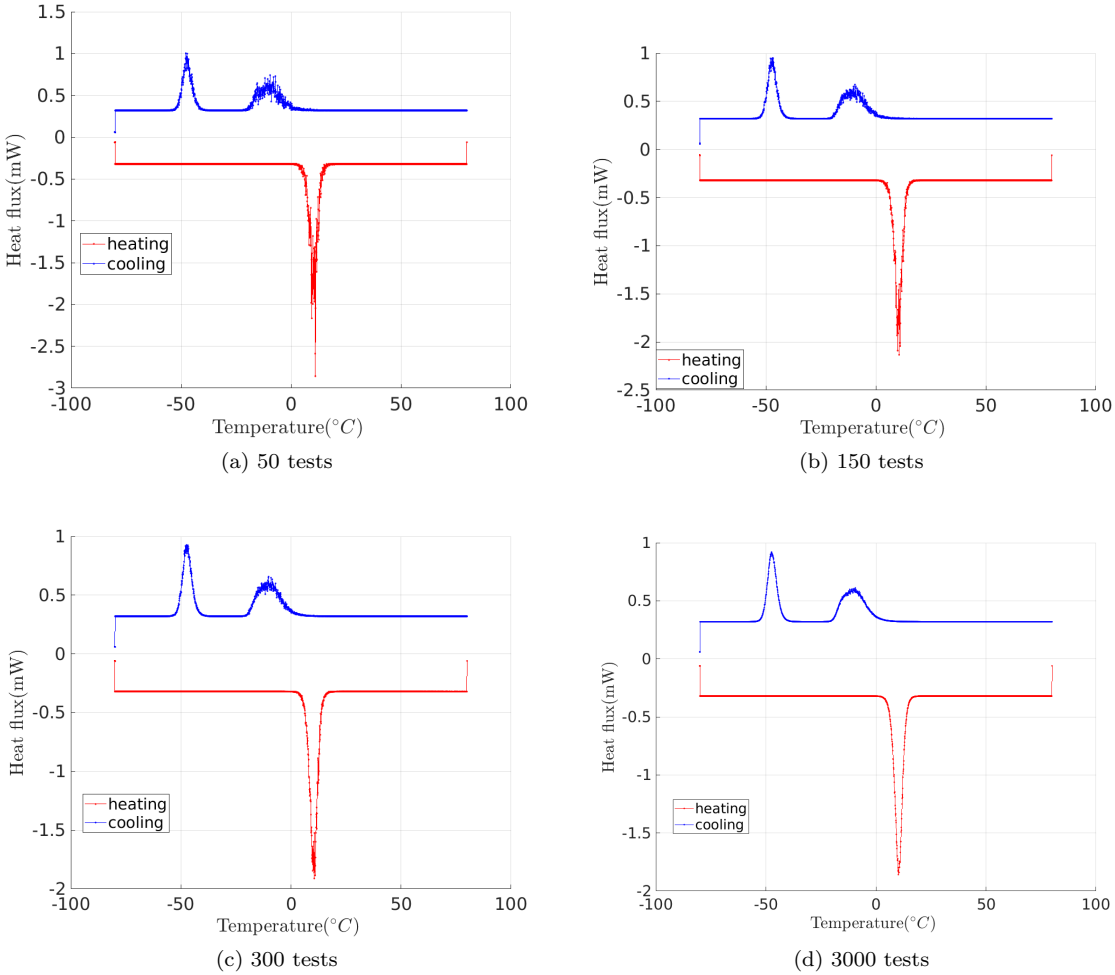

(a) 50 tests

(b) 150 tests

(c) 300 tests

(d) 3000 tests

Figure 25: Relation between convergence and number of independent tests

D Heat equation in the framework of a stochastic approach

The heat equation in the framework of a stochastic approach can be derived as follows. We consider first a simple two phases (1,2) problem so that their volume fraction verifies $f_1 = 1 - \psi$,$f_2 = \psi$ and are consequently only give by parameter ψ. Volume fractions verify:

$$f_1 + f_2 = 1 \tag{99}$$

The equilibrium is supposed to be changed by stress $\boldsymbol{\sigma}$ or temperature T as homogeneous quantities over the volume. Some complementary usual hypotheses are used:

- homogeneous mass density ρ
- homogeneous stiffness $\mathbb{C}$
- homogeneous heat capacity c_p
- homogeneous thermal conductivity κ

Gibbs free energy density of both phases is given by (s_1 and s_2 are written as temperature independent. Results are the same by considering them as temperature dependent):

$$\begin{aligned} \mathfrak{g}1 &= h_1 - Ts_1 - \frac{1}{2}\boldsymbol{\sigma} : \mathbb{C} : \boldsymbol{\sigma} - \boldsymbol{\epsilon}_1^{tr} : \boldsymbol{\sigma} \\ \mathfrak{g}2 &= h_2 - Ts_2 - \frac{1}{2}\boldsymbol{\sigma} : \mathbb{C} : \boldsymbol{\sigma} - \boldsymbol{\epsilon}_2^{tr} : \boldsymbol{\sigma} \end{aligned} \tag{100}$$

The average Gibbs free energy density is simply given by:

$$\mathfrak{g} = f_1\mathfrak{g}1 + f_2\mathfrak{g}2 = \psi(\mathfrak{g}2 - \mathfrak{g}1) + \mathfrak{g}1 \tag{101}$$

leading to:

$$\mathfrak{g} = \psi(\Delta h - T\Delta s - \Delta\boldsymbol{\epsilon}^{tr} : \boldsymbol{\sigma}) + h_1 - Ts_1 - \frac{1}{2}\boldsymbol{\sigma} : \mathbb{C} : \boldsymbol{\sigma} - \boldsymbol{\epsilon}_1^{tr} : \boldsymbol{\sigma} \tag{102}$$

where $\Delta h = h_2 - h_1$, $\Delta s = s_2 - s_1$ and $\Delta\boldsymbol{\epsilon}^{tr} = \boldsymbol{\epsilon}_2^{tr} - \boldsymbol{\epsilon}_1^{tr}$ are the enthalpy density variation, entropy density variation and transformation strain variation respectively. ψ is considered as an internal variable of the macroscopic problem. so that $\mathfrak{g} = \mathfrak{g}(\psi, \boldsymbol{\sigma}, T)$.
Total deformation $\boldsymbol{\epsilon}$, total entropy density s and thermodynamic force X associated with volume fraction ψ are obtained thanks to:

$$\begin{aligned} \boldsymbol{\epsilon} &= -\frac{d\mathfrak{g}}{d\boldsymbol{\sigma}} = \mathbb{C} : \boldsymbol{\sigma} + \psi\Delta\boldsymbol{\epsilon}^{tr} + \boldsymbol{\epsilon}_1^{tr} = f_1\boldsymbol{\epsilon}_1 + f_2\boldsymbol{\epsilon}_2 \\ s &= -\frac{d\mathfrak{g}}{dT} = \psi\Delta s + s_1 = \psi s_2 + (1-\psi)s_1 = f_1 s_1 + f_2 s_2 \\ X &= -\frac{d\mathfrak{g}}{d\psi} = -\Delta h + T\Delta s + \Delta\boldsymbol{\epsilon}^{tr} : \boldsymbol{\sigma} = \mathfrak{g}1 - \mathfrak{g}2 \end{aligned} \tag{103}$$

Indeed, if $X > 0$, the Gibbs free energy density of phase 2 is lower than for phase 1. Transformation is favored leading to an increase of phase 2 associated with phase fraction ψ. This result is formally given by application of the second principle leading to the following intrinsic inequality:

$$-X\dot{\psi} \geq 0 \tag{104}$$

The heat equation (without internal convection) related to this two phases system comes from the application of energy conservation:

$$\frac{du}{dt} = \boldsymbol{\sigma} : \dot{\boldsymbol{\epsilon}} + q_v - \mathrm{div}(\vec{q}_s) \tag{105}$$

where q_v represents the "other" heat sources (that can be considered as zero here since all heat sources are derived from the other terms) and $\vec{q}_s$ is the heat flux vector. The introduction of the decomposition given by Equation 106 with associated variables and the Fourier law (Equation 107) in the energy conservation relationship leads to the heat equation after few calculations (see Equation 108) [11] and [21]).

$$u = \mathfrak{g} + Ts + \boldsymbol{\sigma} : \boldsymbol{\epsilon} \tag{106}$$

$$\vec{q_s} = -\kappa\vec{\nabla}(T) \tag{107}$$

$$\rho c_p \dot{T} = -T\frac{d\boldsymbol{\epsilon}}{dT} : \dot{\boldsymbol{\sigma}} + (X - T\frac{dX}{dT})\dot{\psi} + \kappa\Delta_L T \tag{108}$$

Δ_L indicates a Laplacian operator.

$-T\frac{d\boldsymbol{\epsilon}}{dT} : \dot{\boldsymbol{\sigma}}$ is the so-called *thermoelasticity* heat source term. This term is usually neglected in phase transformation problems leading to few millikelvin temperature increase even in adiabatic conditions (to be compared to dozens of Kelvin given by the second term). It will not be considered in the modeling. Quantity $(X - T\frac{dX}{dT})$ is the so-called *latent heat* denoted as L. It is interesting to observe that this term is composed of the enthalpy density variation and a mechanical energy associated with the transformation strain variation between the two phases:

$$L = X - T\frac{dX}{dT} = h_1 - h_2 - \boldsymbol{\sigma} : (\boldsymbol{\epsilon}_1^{tr} - \boldsymbol{\epsilon}_2^{tr}) \tag{109}$$

In the framework of the stochastic theory developed in the paper, transformation $\mu : i \rightarrow j$ at time step τ is considered. This transition involves two variants (mother and child variants that can belong or not to the same phase) making this situation very close to the two phases situation illustrated above. A specific latent heat L_{ij} can be derived allowing the thermal effect of all possible $i \rightarrow j$ transitions to be estimated. Equation 110 gives this latent heat introduced in the new heat equation valuable at time instant τ for the considered $\mu : i \rightarrow j$ transition.

$$L_{ij} = h_i - h_j - \boldsymbol{\sigma} : (\boldsymbol{\epsilon}_i^{tr} - \boldsymbol{\epsilon}_i^{tr}) \tag{110}$$

The temperature increment associated with time step $\tau = t_n - t_{n-1}$ is simply given by:

$$dT(\tau, \mu) = \frac{1}{\rho c_p} L_{ij} df(\tau, \mu) + \frac{\tau}{\rho c_p}\kappa\Delta_L T \tag{111}$$

References

[1] F. Auricchio and J. Lubliner. A uniaxial model for shape-memory alloys. *International Journal of Solids and Structures*, 34(27):3601 – 3618, 1997.

[2] M. Berny, T. Archer, A. Mavel, P. Beauchêne, S. Roux, and F. Hild. On the analysis of heat haze effects with spacetime dic. *Optics and Lasers in Engineering*, 111:135 – 153, 2018.

[3] T. S. Bording, S. B. Nielsen, and N. Balling. Determination of thermal properties of materials by monte carlo inversion of pulsed needle probe data. *International Journal of Heat and Mass Transfer*, 133:154 – 165, 2019.

[4] A. Bortz, M. Kalos, and J. Lebowitz. A new algorithm for monte carlo simulation of ising spin systems. *Journal of Computational Physics*, 17(1):10 – 18, 1975.

[5] J. Boyd and D. Lagoudas. A thermodynamical constitutive model for shape memory materials. part i. the monolithic shape memory alloy. *International Journal of Plasticity*, 12(6):805 – 842, 1996.

[6] X. Chang, S. Roux, K. Lavernhe-Taillard, and O. Hubert. Phase mapping built from X-ray diffraction mapping spectra, via positive POD algorithm, application to Ni-Ti SMA under uniaxial/biaxial tensile test. *Experimental mechanics*, 2020 submitted.

[7] Y. Chemisky, G. Chatzigeorgiou, P. Kumar, and D. C. Lagoudas. A constitutive model for cyclic actuation of high-temperature shape memory alloys. *Mechanics of Materials*, 68:120 – 136, 2014.

[8] B. Cullity. Elements of x-ray diffraction. *American Journal of Physics*, 25(6):394–395, 1957.

[9] L. Daniel, O. Hubert, N. Buiron, and R. Billardon. Reversible magneto-elastic behavior: A multiscale approach. *Journal of the Mechanics and Physics of Solids*, 56(3):1018 – 1042, 2008.

[10] T. G. Daniel. A general method for numerically simulating the stochastic time evolution of coupled chemical reactions. *Journal of Computational Physics*, 22(4):403 – 434, 1976.

[11] D. Depriester, A. Maynadier, K. Lavernhe-Taillard, and O. Hubert. Thermomechanical modelling of a niti sma sample submitted to displacement-controlled tensile test. *International Journal of Solids and Structures*, 51(10):1901 – 1922, 2014.

[12] M. Fall, O. Hubert, F. Mazaleyrat, K. Lavernhe-Taillard, and A. Pasko. A multiscale modeling of magnetic shape memory alloys: Application to nimnga single crystal. *IEEE Transactions on Magnetics*, 52(5):1–4, May 2016.

[13] M. D. Fall, E. Patoor, O. Hubert, and K. Lavernhe-Taillard. Comparative study of two multiscale thermomechanical models of polycrystalline shape memory alloys: Application to a representative volume element of titanium–niobium. *Shape Memory and Superelasticity*, 5(2):163–171, Jun 2019.

[14] K. Gall, H. Sehitoglu, R. Anderson, I. Karaman, Y. I. Chumlyakov, and I. V. Kireeva. On the mechanical behavior of single crystal niti shape memory alloys and related polycrystalline phenomenon. *Materials Science and Engineering: A*, 317(1):85 – 92, 2001.

[15] G. Helbert, L. Dieng, S. A. Chirani, L. Saint-Sulpice, T. Lecompte, S. Calloch, and P. Pilvin. Investigation of niti based damper effects in bridge cables vibration response: Damping capacity and stiffness changes. *Engineering Structures*, 165:184 – 197, 2018.

[16] H. Huang, B. Durand, Q. Sun, and H. Zhao. An experimental study of niti alloy under shear loading over a large range of strain rates. *International Journal of Impact Engineering*, 108:402 – 413, 2017. In Honour of the Editor-in-Chief, Professor Magnus Langseth, on his 65th Birthday.

[17] R. James and K. Hane. Martensitic transformations and shape-memory materials. *Acta Materialia*, 48(1):197 – 222, 2000.

[18] D. Lagoudas, Y. Chemisky, G. Chatzigeorgiou, and F. Meraghni. Modeling of coupled phase transformation and reorientation in shape memory alloys under non-proportional thermomechanical loading. *International Journal of Plasticity*, 82:192 – 224, 2016.

[19] D. Lagoudas, P. Entchev, P. Popov, E. Patoor, L. Brinson, and X. Gao. Shape memory alloys, part ii: Modeling of polycrystals. *Mechanics of Materials*, 38(5-6):430–462, 5 2006.

[20] K. Lavernhe-Taillard, S. Calloch, S. Arbab-Chirani, and C. Lexcellent. Multiaxial shape memory effect and superelasticity. *Strain*, 45(1):77–84, 2009.

[21] J. Lemaitre and J.-L. Chaboche. *Mechanics of Solid Materials*. Cambridge University Press, 1990.

[22] C. Lexcellent and P. Blanc. Phase transformation yield surface determination for some shape memory alloys. *Acta Materialia*, 52(8):2317 – 2324, 2004.

[23] C. Lexcellent, M. Boubakar, C. Bouvet, and S. Calloch. About modelling the shape memory alloy behaviour based on the phase transformation surface identification under proportional loading and anisothermal conditions. *International Journal of Solids and Structures*, 43(3):613 – 626, 2006.

[24] C. Lexcellent, A. Vivet, C. Bouvet, S. Calloch, and P. Blanc. Experimental and numerical determinations of the initial surface of phase transformation under biaxial loading in some polycrystalline shape-memory alloys. *Journal of the Mechanics and Physics of Solids*, 50(12):2717 – 2735, 2002.

[25] C. Liang and C. A. Rogers. One-dimensional thermomechanical constitutive relations for shape memory materials. *Journal of Intelligent Material Systems and Structures*, 8(4):285–302, 1997.

[26] A. Maynadier, D. Depriester, K. Lavernhe-Taillard, and O. Hubert. Thermo-mechanical description of phase transformation in ni-ti shape memory alloy. *Procedia Engineering*, 10:2208 – 2213, 2011. 11th International Conference on the Mechanical Behavior of Materials (ICM11).

[27] A. Maynadier, M. Poncelet, K. Lavernhe-Taillard, and S. Roux. One-shot measurement of thermal and kinematic fields: Infrared image correlation (iric). *Experimental Mechanics*, 52(3):241–255, 2012. cited By 32.

[28] P. McCormick, Y. Liu, and S. Miyazaki. Intrinsic thermal-mechanical behaviour associated with the stress-induced martensitic transformation in niti. *Materials Science and Engineering: A*, 167(1):51 – 56, 1993 .

[29] K. Otsuka and C. Wayman. *Shape memory materials*. Cambridge university press, 1999.

[30] E. Patoor, D. C. Lagoudas, P. B. Entchev, L. C. Brinson, and X. Gao. Shape memory alloys, part i: General properties and modeling of single crystals. *Mechanics of Materials*, 38(5):391 – 429, 2006. Shape Memory Alloys.

[31] B. Peultier, T. B. Zineb, and E. Patoor. Macroscopic constitutive law for sma: Application to structure analysis by fem. *Materials Science and Engineering: A*, 438-440:454 – 458, 2006. Proceedings of the International Conference on Martensitic Transformations.

[32] W. Reiher. Hammersley, j. m., d. c. handscomb: Monte carlo methods. methuen & co., london, and john wiley & sons, new york, 1964. vii + 178 s., preis: 25 s. *Biometrische Zeitschrift*, 8(3):209–209, 1966.

[33] J. Shaw and S. Kyriakides. Thermomechanical aspects of niti. *Journal of the Mechanics and Physics of Solids*, 43(8):1243 – 1281, 1995.

[34] J. Shaw and S. Kyriakides. On the nucleation and propagation of phase transformation fronts in a niti alloy. *Acta Materialia*, 45(2):683 – 700, 1997.

[35] N. Siredey, E. Patoor, M. Berveiller, and A. Eberhardt. Constitutive equations for polycrystalline thermoelastic shape memory alloys.: Part i. intragranular interactions and behavior of the grain. *International Journal of Solids and Structures*, 36(28):4289 – 4315, 1999.

[36] Y. Soejima, S. Motomura, M. Mitsuhara, T. Inamura, and M. Nishida. In situ scanning electron microscopy study of the thermoelastic martensitic transformation in ti–ni shape memory alloy. *Acta Materialia*, 103:352 – 360, 2016.

[37] A. Sommerfeld, F. Bopp, and J. Meixner. *Thermodynamics and Statistical Mechanics.* Lectures on theoretical physics. Academic Press, 1964.

[38] Q. Sun and Y. He. A multiscale continuum model of the grain-size dependence of the stress hysteresis in shape memory alloy polycrystals. *International Journal of Solids and Structures*, 45(13):3868 – 3896, 2008. Special Issue Honoring K.C. Hwang.

[39] X. Zhang and H. Sehitoglu. Crystallography of the b2 $\rightarrow$ r $\rightarrow$ b19' phase transformations in niti. *Materials Science and Engineering: A*, 374(1):292 – 302, 2004.